FAST TRAINING OF SINUSOIDAL NEURAL FIELDS VIA SCALING INITIALIZATION

Taesun Yeom; Sangyoon Lee* & Jaeho Lee † POSTECH

{tsyeom, sangyoon.lee, jaeho.lee}@postech.ac.kr

ABSTRACT

Neural fields are an emerging paradigm that represent data as continuous functions parameterized by neural networks. Despite many advantages, neural fields often have a high training cost, which prevents a broader adoption. In this paper, we focus on a popular family of neural fields, called sinusoidal neural fields (SNFs), and study how it should be initialized to maximize the training speed. We find that the standard initialization scheme for SNFs—designed based on the signal propagation principle—is suboptimal. In particular, we show that by simply multiplying each weight (except for the last layer) by a constant, we can accelerate SNF training by $10\times$. This method, coined *weight scaling*, consistently provides a significant speedup over various data domains, allowing the SNFs to train faster than more recently proposed architectures. To understand why the weight scaling works well, we conduct extensive theoretical and empirical analyses which reveal that the weight scaling not only resolves the spectral bias quite effectively but also enjoys a well-conditioned optimization trajectory.

1 Introduction

Neural field (NF) is a special family of neural networks designed to represent a single datum (Xie et al., 2022). Precisely, NFs parametrize each datum with the weights of a neural net which is trained to fit the mapping from spatiotemporal coordinates to corresponding signal values. Thanks to their versatility and low memory footprint, NFs have been rapidly adopted in various domains, including high-dimensional computer vision and graphics (Sitzmann et al., 2019; Mildenhall et al., 2020; Poole et al., 2023), physics-informed machine learning (Wang et al., 2021; Serrano et al., 2023), robotics (Simeonov et al., 2022), and non-Euclidean signal processing (Rebain et al., 2024).

For neural fields, the *training speed* is of vital importance. Representing each datum as an NF requires tedious training of a neural network, which can take up to several hours of GPU-based training (Mildenhall et al., 2020). This computational burden becomes a critical obstacle toward adoption to tasks that involve large-scale data, such as NF-based inference or generation (Ma et al., 2024; Papa et al., 2024). To address this issue, many research efforts have been taken to accelerate NF training, including fast-trainable NF architectures (Sitzmann et al., 2020b; Müller et al., 2022), meta-learning (Sitzmann et al., 2020a; Chen & Wang, 2022), and data transformations (Seo et al., 2024).

Despite such efforts, a critical aspect of NF training remains understudied: How should we *initialize* NFs for the fastest training? While the importance of a good initialization has been much contemplated in classic deep learning literature (Glorot & Bengio, 2010; Zhang et al., 2019), such understandings do not immediately answer our question, for many reasons. First, conventional works mostly focus on how initialization affects the signal propagation properties of deep networks with hundreds of layers, while most NFs use shallow models with only a few layers (Mildenhall et al., 2020). Second, conventional works aim to maximize the model quality at convergence, while in NFs it is often more important how fast the network achieves certain fidelity criterion (Müller et al., 2022). Lastly, NFs put great emphasis on how the model performs on seen inputs (*i.e.*, training loss)

^{*}Equal contribution.

[†]Corresponding author.

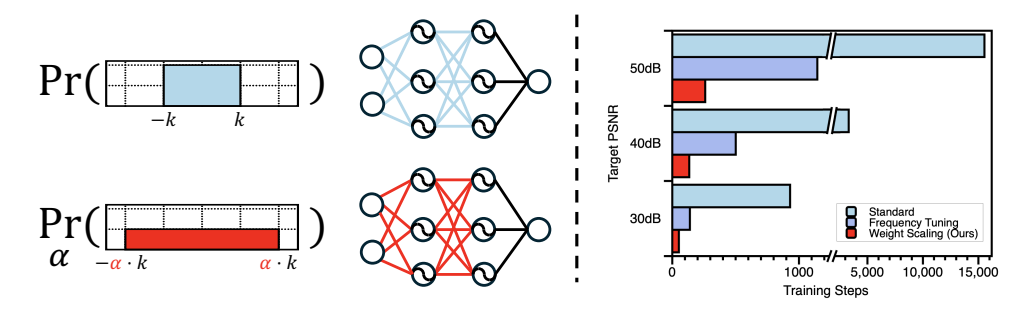


Figure 1. A simple weight scaling accelerates training. The proposed weight scaling scales up the initial weights of an SNF by the factor of α , except for the last layer (left panel). This scaling significantly reduces the number of steps required to achieve the desired level of training loss (right panel).

and leaves how well it interpolates between coordinates (i.e., generalizability) as a secondary issue, while conventional neural networks care exclusively on the test performance.

To fill this gap, in this paper, we investigate how the initialization affects the training efficiency of neural fields. In particular, we focus on initializing *sinusoidal neural field* (SNF) architectures, *i.e.*, multilayer perceptrons with sinusoidal activation functions (Sitzmann et al., 2020b). SNF is one of the most widely used NFs, due to its versatility and parameter-efficiency; the architecture works as a strong baseline in a wide range of data modalities (Grattarola & Vandergheynst, 2022; Kim et al., 2024; Rußwurm et al., 2024) and is used as an indispensable building block of many state-of-the-art neural field frameworks (Guo et al., 2023; Schwarz et al., 2023; Pal et al., 2024).

Contribution. We first discover that the current practice of SNF initialization is highly suboptimal in terms of the training speed (Sitzmann et al., 2020b). Precisely, we find that one can accelerate the training speed of SNFs by up to $10\times$, simply by scaling up the initial weights of all layers by a well-chosen factor. This extremely simple tuning, coined weight scaling (WS), provides a much greater speedup than the conventional SNF tuning strategy, i.e., scaling up the frequency multiplier of the activation functions (called ω_0 in Sitzmann et al. (2020b)). Furthermore, this speedup can be achieved without any degradation in the generalization capabilities of the model, if we keep the scaling factor at a moderate level. Interestingly, experiments suggest that the optimal scaling factor, which strikes the balance between speedup and generalization, mainly depends on the physical scale of the NF workload (e.g., data resolution and model size) and remains similar over different data.

To demystify why the weight scaling accelerates the SNF training, we conduct an in-depth analysis. In particular, we focus on understanding how the effects of WS on SNFs are similar yet different from ReLU nets, where the so-called *lazy training* phenomenon takes place (Chizat et al., 2019)—weight-scaled ReLU nets behave similarly to kernels, enjoying exponential convergence in theory for shallow nets but failing to achieve good accuracy at practical scales due to ill-conditioned trajectories. Our theoretical and empirical analyses highlight several key differences that sinusoidal activations bring, such as: (1) Weight-scaled SNFs also preserve activation distributions over layers, facilitating the gradient propagation when training a deep model (Proposition 3.1). (2) Weight scaling increases not only the frequency of each basis, but also increases the relative magnitude of higher-order harmonics, which helps fit the high-frequency components abundant in natural signals (Lemma 4.2 and Section 4.2). (3) Weight-scaled SNFs enjoy even better-conditioned trajectories than the unscaled models, as captured by the eigenspectrum analysis (Section 4.3).

In a sense, our study constitutes a call for rethinking the role of the initialization for neural fields, by demonstrating how dramatically suboptimal the current schemes can be in key performance metrics for NFs. We hope that our work will further inspire more sophisticated initialization algorithms.

2 RELATED WORK

Training efficiency of neural fields. There are two prevailing strategies to accelerate NF training. The first approach is to adopt advanced NF architectures, which mitigate the spectral bias of neural nets that hinders fitting high-frequency signals (Rahaman et al., 2019; Xu et al., 2020). Popular examples include utilizing specially designed positional encodings (Tancik et al., 2020; Müller et al., 2022) or activation functions (Sitzmann et al., 2020b; Ramasinghe & Lucey, 2022; Liu et al., 2024).

Another strategy is to amortize the training cost via meta-learning, *e.g.*, by training a fast-trainable initialization (Sitzmann et al., 2020a; Tancik et al., 2021) or constructing an auxiliary model that predicts NF parameters from the datum (Chen & Wang, 2022). This work aims to accelerate NF training through a better initialization. Unlike meta-learned initializations, however, our aim is to understand how the initialization (its scale, specifically) can facilitate training by analyzing how it affects optimization dynamics, without meta-learning involved.

Neural network initialization. Early works on network initialization focus on preserving the signals through layers to facilitate training deep networks. This is typically done via principled scaling of the initial weights (Glorot & Bengio, 2010; He et al., 2015), or by ensuring isometries in each layer through orthogonalization (Xiao et al., 2018). Recent works focus on the relationship between the initialization and the implicit bias of SGD (Vardi, 2023). In particular, the initialization scale determines whether the training takes place in the *rich* regime or *kernel* regime, which correspond to stronger and weaker influence of implicit bias, respectively (Woodworth et al., 2020; Varre et al., 2023). Empirically, weak implicit bias leads to the models trained from larger initialization to generalize poorly (Mehta et al., 2021). Our analyses share some spirit with the latter line of the literature. Distinct from the works, however, we put our main focus on how initialization affects the training speed, specifically targeting the neural fields.

Initializing sinusoidal neural fields. There is a limited number of works that study the initialization for SNFs. Sitzmann et al. (2020b) proposes an initialization scheme for SNF, designed in the signal propagation perspective. Tancik et al. (2021) develops a meta-learning algorithm to learn initializations for SNFs. Lee et al. (2021) extends the algorithm for sparse networks. Most related to our work, Saratchandran et al. (2024) proposes an initialization scheme that aims to facilitate the parameter-efficiency of SNFs. Different from this work, our work primarily focuses on the training efficiency, and achieves much faster training speed empirically.

3 NEURAL FIELDS INITIALIZATION VIA WEIGHT SCALING

In this section, we formally describe the weight scaling for a sinusoidal neural field initialization, and briefly discuss the theoretical and empirical properties of the method.

3.1 Network setup and notations

We begin by introducing the necessary notations and problem setup. A sinusoidal neural field is a multilayer perceptron (MLP) with sinusoidal activation functions (Sitzmann et al., 2020b). More concretely, suppose that we have an input $X \in \mathbb{R}^{d_0 \times N}$, where N is the number of d_0 -dimensional coordinates. Then, an l-layer SNF can be characterized recursively via:

$$f(X; \mathbf{W}) = W^{(l)} Z^{(l-1)} + b^{(l)}, \qquad Z^{(i)} = \sigma_i (W^{(i)} Z^{(i-1)} + b^{(i)}), \quad i \in [l-1],$$
 (1)

parametrized by $\mathbf{W} = (W^{(1)}, b^{(1)}, \dots, W^{(l)}, b^{(l)})$, where each $W^{(i)} \in \mathbb{R}^{d_i \times d_{i-1}}$ denotes the weight matrix, $b^{(i)} \in \mathbb{R}^{d_i}$ denotes the bias, and $Z^{(i)} \in \mathbb{R}^{d_i \times N}$ denotes the activation of the ith layer. Here, we let $Z^{(0)} = X$, and the activation function $\sigma_i : \mathbb{R}^{d_i} \to \mathbb{R}^{d_i}$ are the sinusoidal activations applied entrywise, with some frequency multiplier ω . The standard practice is to use a different frequency multiplier for the first layer. Precisely, we apply the activation function $\sigma_1(x) = \sin(\omega_0 \cdot x)$ for the first layer, and $\sigma_i(x) = \sin(\omega_b \cdot x)$ for all other layers, i.e., $i \neq 1$.

The SNF is trained using the gradient descent, with the mean-squared error (MSE) as a loss function. We assume that the input coordinates of the training data (*i.e.*, the column vectors of the input data) have been scaled to lie inside the hypercube $[-1, +1]^{d_0}$, as in Sitzmann et al. (2020b).

3.2 STANDARD INITIALIZATION

The standard initialization scheme for the sinusoidal neural fields independently draws each weight entry from a random distribution (Sitzmann et al., 2020b). Precisely, the weight matrices are initialized according to the scaled uniform distribution as

$$w_{j,k}^{(1)} \stackrel{\text{i.i.d.}}{\sim} \text{Unif}\left(-\frac{1}{d_0}, \frac{1}{d_0}\right), \qquad w_{j,k}^{(i)} \stackrel{\text{i.i.d.}}{\sim} \text{Unif}\left(-\frac{\sqrt{6}}{\omega_h \sqrt{d_{i-1}}}, \frac{\sqrt{6}}{\omega_h \sqrt{d_{i-1}}}\right),$$
 (2)

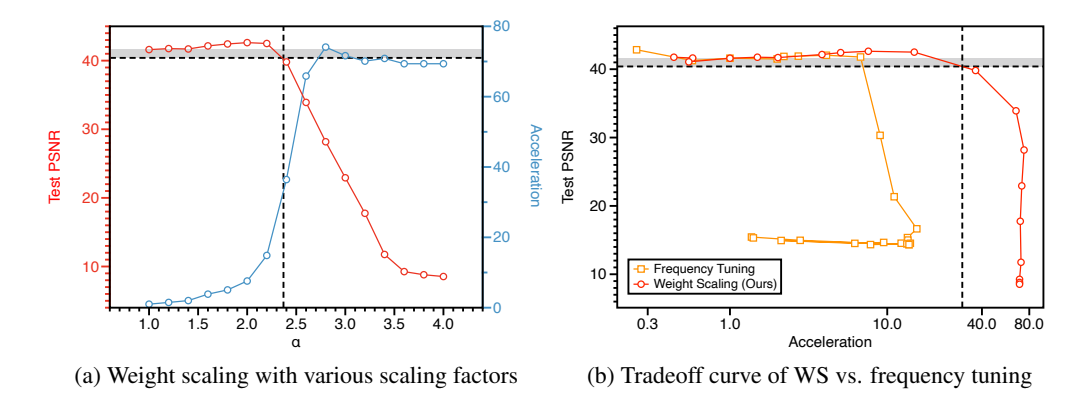


Figure 2. Scaling factors and the speed-generalization tradeoff. (a) As we increase the scaling factor α , the training speed (\circ) tends to become faster while the interpolation performance (\circ) gets lower. Notably, however, there exists some range of α where we enjoy acceleration with negligible degradation in test PSNR. (b) Comparing with the frequency tuning (\square), the weight scaling (\circ) achieves a better tradeoff.

where $w_{j,k}^{(i)}$ denotes the (j,k)-th entry of the ith layer weight matrix $W^{(i)}$.

Importantly, the range of the uniform initialization (Eq. (2)) is determined based on the *distribution* preserving principle, which aims to make the distribution of the activation Z_i similar throughout all layers. In particular, Sitzmann et al. (2020b, Theorem 1.8) formally proves that the choice of the numerator (i.e., $\sqrt{6}$) ensures the activation distribution to be constantly $\arcsin(-1,1)$ throughout all hidden layers of the initialized sinusoidal neural field.

Frequency tuning. A popular way to tune the initialization (Eq. (2)) for the given data is by modifying the frequency multiplier of the first layer ω_0 . This method, which we call *frequency tuning*, affects the frequency spectrum of the initial SNF, enhancing the fitting of signals within certain frequency range. It is not typical to tune ω_h , as changing its value does not change the initial SNF; the effects are cancelled out by the scaling factors in the initialization scheme.

3.3 Initialization with weight scaling

In this paper, we develop a simple generalization of the standard initialization scheme. In particular, we consider *weight scaling*, which multiplies a certain scaling factor $\alpha \geq 1$ to the initialized weights in all layers except for the last layer. More concretely, the initialization scheme is

$$w_{j,k}^{(1)} \stackrel{\text{i.i.d.}}{\sim} \text{Unif}\left(-\frac{\alpha}{d_0}, \frac{\alpha}{d_0}\right), \qquad w_{j,k}^{(i)} \stackrel{\text{i.i.d.}}{\sim} \text{Unif}\left(-\frac{\alpha\sqrt{6}}{\omega_h\sqrt{d_{i-1}}}, \frac{\alpha\sqrt{6}}{\omega_h\sqrt{d_{i-1}}}\right),$$
 (3)

where we let $\alpha=1$ for the last layer; this design is due to the fact that any scaling in the last layer weight leads to a direct scaling of the initial function $f\mapsto \alpha f$, which is known to be harmful for the generalizability, according to the theoretical work of Chizat et al. (2019). Empirically, we observe that this weight scaling is much more effective in speeding up the training than a recently proposed variant which scales up only the last layer of the NF (Saratchandran et al., 2024); see Section 5.

There are two notable characteristics of the weight-scaled initializations.

(1) **Distribution preservation.** An attractive property of the proposed weight scaling is that, for SNFs, any $\alpha \ge 1$ also preserves the activation distribution over the layers. In particular, we provide the following result, which shows that the activation distributions will still be an $\arcsin(-1,1)$.

Proposition 3.1 (Informal; extension of Sitzmann et al. (2020b, Theorem 1.8)). *Consider an l-layer SNF initialized with the weight scaling (Eq.* (3)). For any $\alpha \geq 1$, we have, in an approximate sense,

$$Z^{(i)} \sim \arcsin(-1, 1), \quad \forall i \in \{2, \dots, l-1\}.$$
 (4)

The detailed statement of this proposition and the numerical derivation will be given in Appendix A.

¹This point has also been noted in Sitzmann et al. (2020b), but has not been discussed quantitatively for $\alpha \ge 1$. We make this point concrete via numerical analyses on the large α case.

The proposition implies that we can tune the scaling factor α within the range $[1, \infty)$ without any concerns regarding preserving the forward propagation signal. Thus, we can safely adopt the weight scaling for training a very deep sinusoidal neural field.

(2) **Speed vs. generalization.** Empirically, we observe that the weight scaling (Eq. (3)) allows us to explore for the "sweet spot" region, where we can enjoy the accelerated training, while not suffering from any degradation in the generalization performance on unseen coordinates.

The Fig. 2 illustrates this phenomenon for the case of image regression, where we train an SNF to fit a downsampled image until some desired peak signal-to-noise ratio (PSNR) is met, and then use the model to interpolate between seen pixel coordinates.

We observe that by increasing α from 1, the loss on unseen coordinates increase, and the training speed increases as well. Notably, there exists some $\alpha>1$ where the test PSNR remains similar while the training speed has strictly increased.

3.4 THE PARADIGM OF EFFICIENCY-ORIENTED INITIALIZATION

The latter phenomenon motivates us to develop an alternative perspective on a goodness of a neural field initialization, which may replace or be used jointly with the distribution preservation principle. More specifically, we consider an optimization problem

$$\max_{\alpha \ge 1} \operatorname{speed}(\alpha)/\operatorname{speed}(1) \quad \operatorname{subject to} \quad \operatorname{TestLoss}(\alpha) - \operatorname{TestLoss}(1) \le \varepsilon, \tag{5}$$

where speed(α) denotes the training speed (e.g., a reciprocal of the number of steps required) of SNF when initialized with α weight scaling, and $\text{TestLoss}(\alpha)$ denotes the loss on the unseen coordinates when trained from the initialization. Given this objective, the key questions we try to address are:

- Why does the weight scaling accelerate the training of SNFs?

 > See Section 4
- Is weight scaling generally applicable for other data modalities?

 ▷ See Section 5.1
- How can we select a good α , without expensive per-datum tuning? \triangleright See Section 5.2

4 Understanding the effects of the weight scaling

We now take a closer look at the weight scaling to understand how it speeds up the training of sinusoidal neural fields. Before diving deeper into our analyses, we first discuss why a conventional understanding does not fully explain the phenomenon we observed for the case of SNF.

Comparison with lazy training. At the first glance, it is tempting to argue that this phenomenon is connected to the "lazy training" phenomenon (Chizat et al., 2019; Woodworth et al., 2020): Scaling the initial weights ($\mathbf{W} \mapsto \alpha \mathbf{W}$) amplifies the initial model functional ($f \mapsto \alpha^l f$), which in turn leads to the model to be linearized; then, one can show that the SGD converges at an exponential rate, *i.e.*, the fast training, with the trained parameters being very close to the initial one. However, there is a significant gap between this theoretical understanding and our observations for the SNFs:

- The proposed weight scaling does not amplify the initial functional, as sinusoidal activations are not positively homogeneous (i.e., $\sigma(ax) \neq a \cdot \sigma(x)$), even for positive a, x), unlike ReLU. In fact, WS keeps the last layer parameters unscaled, making it further from any functional amplification, and empirically works better than a direct amplification of functional (Saratchandran et al., 2024).
- At a practical scale, a naïve scaling of initial weights for ReLU networks leads to both high training and test losses, due to a high condition number (Chizat et al., 2019, Appendix C). In contrast, the training loss of the WS remains very small even at the practical tasks.

In light of these differences, we provide alternative theoretical and empirical analyses that can help explain why the WS accelerates training, unlike in ReLU nets. In particular, we reveal that:

- WS on SNFs has two distinctive effects from ReLU nets, in terms of the initial functional and the layerwise learning rate; the former is the major contributor to the acceleration (Section 4.1).
- At initialization, WS increases both (1) the frequency of each basis, and (2) the relative power of the high-frequency bases (Section 4.2).
- WS also results in a better-conditioned optimization trajectory (Section 4.3).

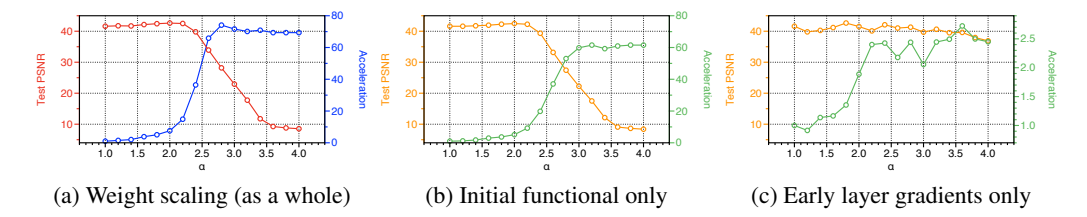


Figure 3. **Decoupling the effects of weight scaling on SNF.** We decouple the effect of weight scaling on how it amplifies the early layer gradients, from the effects of having a higher-frequency initial functional. We observe that the initial functional itself plays the key role, resulting in a much greater acceleration.

4.1 Two effects of weight scaling on sinusoidal networks

There are two major differences in how the weight scaling impacts SNF training compared to its effect on conventional neural networks with positive-homogeneous activation functions, *e.g.*, ReLU. (1) *Initial functional*: Larger weights lead to higher frequency (low-level) features in SNF, whereas in ReLU nets scaling up does not change the neuronal directions (more discussions in Section 4.2). (2) *Larger early layer gradients*: Unlike ReLU nets, scaling up SNF weights has a disproportionate impact on the layerwise gradients; earlier layers receive larger gradients (see remarks below).

Motivated by this insight, we compare which of these two elements play a dominant role in speeding up the SNF training by decoupling these elements (Fig. 3). In particular, we analyze how changing only the initial weights—with the layerwise learning rates that are scaled down to match the rates of unscaled SNF—affects the speed-generalization tradeoff; we also compare with the version where the initial function stays the same as default, but the learning rates on early layers are amplified. From the results, we observe that the effect of having a good initial functional, with rich high-frequency functions, play a dominant role on speeding up the SNF training. The disproportionate learning rate also provides a mild speedup, while requiring less sacrifice in the generalizability.

How are the early layer gradients amplified? Essentially, this is also due to the lack of positive-homogeneity of the activation function. To see this, consider a toy two-layer neural net with width one $f(x) = w^{(2)}\sigma(w^{(1)}x)$. The loss gradient for each layer weight is proportional to the layerwise gradients of the function, which is $\nabla_{\mathbf{w}} f = \left(w^{(2)}x\sigma'(w^{(1)}x), \sigma(w^{(1)}x)\right)$. For ReLU activations, both entries of $\nabla_{\mathbf{w}} f$ grow linearly as we increase the scale of both weights. For sin activations, on the other hand, the first entry scales linearly, but the scale of the second entry remains the same. Following a similar line of reasoning, we can show that the first layer of a depth-l sinusoidal network has a gradient that scales as α^l , while the last layer gradient scales as 1. We provide a more detailed discussion on the α -dependency of layerwise gradients in Appendix B.3.

4.2 Frequency spectrum of the initial functional

We have seen that the initial functional has a profound impact on the training speed, but how does the weight scaling affect the functional? The answer is easy for two-layer nets; the weight scaling amplifies the frequency of each hidden layer neuron, enabling the model to cover wider frequency range with hardly updating the *features* generated by the first layer.

How about for deeper networks? Our theoretical and empirical analyses reveals that, for deeper SNFs, the weight scaling also increases the *relative power* of the higher-frequency bases. Thus, the weight-scaled networks may suffer less from the spectral bias, and can easily represent signals with large high-frequency components (Rahaman et al., 2019).

Theoretical analysis. We now show theoretically that the weight scaling increases the relative power of the higher-frequency bases. For simplicity, consider again a three-layer bias-free SNF

$$f(x; \mathbf{W}) = W^{(3)} \sin(W^{(2)} \sin(W^{(1)} x)), \tag{6}$$

with sinusoidal activation functions. Then, it can be shown that the overall frequency spectrum of the function $f(\cdot; \mathbf{W})$ can be re-expressed as the multiples of the first layer frequencies, via Fourier series expansion and the Jacobi-Anger identity (Yüce et al., 2022).

Lemma 4.1 (Corollary of Yüce et al. (2022)). The network Eq. (6) can be rewritten as

$$f(x; \mathbf{W}) = 2W^{(3)} \sum_{\ell \in \mathbb{Z}_{odd}} J_{\ell}(W^{(2)}) \sin(\ell W^{(1)} x), \tag{7}$$

where $J_{\ell}(\cdot)$ denotes the Bessel function (of the first kind) with order ℓ .

Given the Bessel form (7), let us proceed to analyze the effect of weight scaling. By scaling the first layer weight, i.e., $W^{(1)} \mapsto \alpha W^{(1)}$, we are increasing the frequencies of each sinusoidal basis by the factor of α . That is, each frequency basis becomes a higher-frequency sinusoid.

Scaling the second layer weight, on the other hand, acts by affecting the magnitude of each sinusoidal basis, *i.e.*, $J_{\ell}(W^{(2)})$. For this quantity, we can show that the rate that the Bessel function coefficients evolve as we consider a higher order harmonics (*i.e.*, larger ℓ) scales at the speed proportional to α^2 . That is, the relative power of the higher-order harmonics becomes much greater as we consider larger scaling factor α . To formalize this point, let us further simplify the model (6) to have width one. Then, we can prove the following sandwich bound:

Lemma 4.2 (Scaling of harmonics). For any nonzero $W^{(2)} \in (-\pi/2, \pi/2)$, we have:

$$\frac{(W^{(2)})^2}{(2\ell+2)(2\ell+4)} < \frac{J_{\ell+2}(W^{(2)})}{J_{\ell}(W^{(2)})} < \frac{(W^{(2)})^2}{(2\ell+1)(2\ell+3)}.$$
 (8)

In other words, replacing $W^{(2)} \mapsto \alpha \cdot W^{(2)}$ increases the growth rate $J_{\ell+2}/J_{\ell}$ by α^2 . We note that there exists a restriction in the range $W^{(2)}$ which prevents us from considering very large α . However, empirically, we observe that such amplification indeed takes place for the practical ranges of α where the generalization performance remains similar.

Summing up, the weight scaling has two effects on SNFs with more than two layers. First, the WS increases the frequencies of each sinusoidal basis by scaling the first layer weights. Second, the WS increases the relative weight of higher-frequency sinusoidal bases, by scaling the weight matrices of the intermediate layers.

Empirical analysis. To demonstrate that the increase of coefficients in the higher-order harmonics takes place indeed, we conduct a spectral analysis of an initialized SNF for audio data (Fig. 4). From the plot, we observe that the initialized SNFs with larger scaling factor α has a richer higher frequency spectrum. Moreover, the decay rate of the higher-frequency components, as we consider

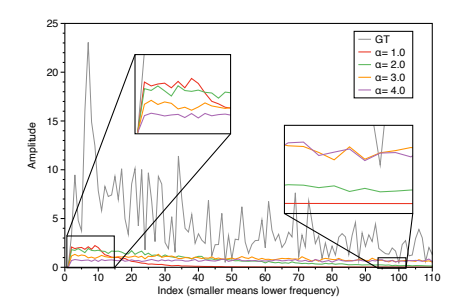


Figure 4. **Spectrum of initialized SNFs.** 1D-FFT of an initialized 5-layer SNF, with various levels of weight scaling factors.

increase the frequency level, is much smaller for larger α ; as a consequence, weight-scaled SNFs tend to have non-zero coefficients for very high frequency ranges, enabling a faster fitting to the natural audio signals (gray) with rich high-frequency components.

4.3 OPTIMIZATION TRAJECTORIES OF WEIGHT-SCALED NETWORKS

Now, we study the optimization properties of SNFs through the lens of the empirical neural tangent kernel (eNTK). We empirically analyze two properties of the eNTK eigenspectrum of the SNF, which are relevant to the training speed: (1) *condition number*, and (2) *kernel-task alignment*.

Condition number. Roughly, the condition number denotes the ratio $\lambda_{\rm max}/\lambda_{\rm min}$ of the largest and the smallest eigenvalues of the eNTK; this quantity determines the exponent of the exponential convergence rates of the kernelized models, with larger condition number meaning the slower training (Chizat et al., 2019). In Fig. 5a, we plot how the condition numbers of the eNTK evolve during the training for SNFs, under weight scaling or frequency tuning; for numerical stability, we take an average of top-5 and bottom-5 eigenvalues and take their ratio. We observe that the weight-scaled SNFs tend to have a much smaller condition number at initialization, which becomes even smaller during the training. On the other hand, the SNF initialized with the standard initialization scheme suffers from a very high condition number, which gets even higher during the training.

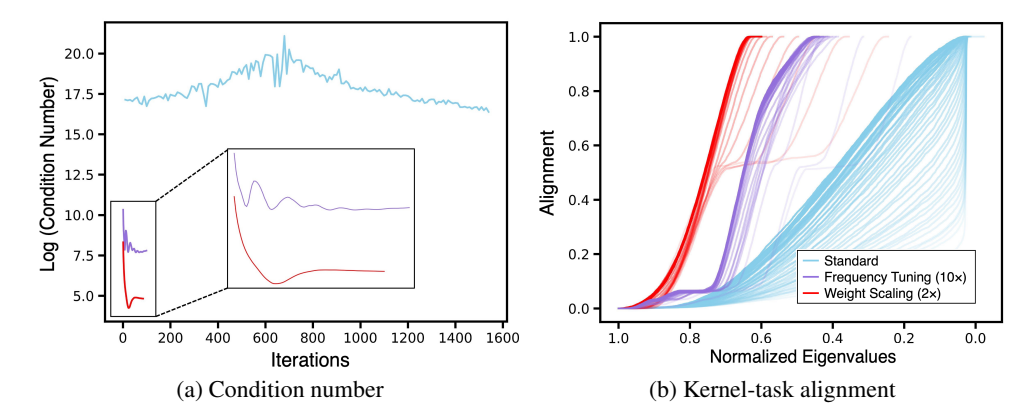


Figure 5. **Eigenanalyses with eNTK.** (a) Weight scaling improves the conditioning of the SNF optimization at all SGD steps, greatly reducing the condition number. (b) Weight-scaled SNF enjoys a better kernel-task alignment throughout the training; darker lines indicate later iterations.

Table 1. **Weight scaling in various data domains.** We compare the training speed of the weight-scaled SNF against other baselines in various data domains. To evaluate the training speed, we train for a fixed number of steps and compare the training loss achieved. **Bold** denotes the best option, and <u>underlined</u> denotes the runner-up. We have experimented with five random seeds, and report the mean and the standard deviation.

		Image (PSNR)		Occ. Field (IoU)	Spherical (PSNR)	Audio (PSNR)
	Activation	KODAK	DIV2K	Lucy	ERA5	Bach
Xavier Uniform (Glorot & Bengio, 2010)	Sinusoidal	0.46±0.10	0.39 ± 0.10	0.0000 ± 0.0000	4.11±0.66	7.77±0.20
ReLU + P.E. (Mildenhall et al., 2020)	ReLU	18.60 ± 0.08	16.72 ± 0.08	0.9896 ± 0.0003	33.30 ± 0.54	24.98 ± 0.19
FFN (Tancik et al., 2020)	ReLU	20.52 ± 0.60	19.81 ± 0.48	0.9843 ± 0.0020	38.69 ± 0.27	16.66 ± 0.28
SIREN init. (Sitzmann et al., 2020b)	Sinusoidal	24.58 ± 0.05	22.86 ± 0.06	0.9925 ± 0.0001	38.72 ± 0.07	37.37 ± 3.11
GaussNet (Ramasinghe & Lucey, 2022)	Gaussian	21.94 ± 2.48	19.22 ± 0.14	0.9914 ± 0.0005	38.56 ± 0.51	$\overline{27.47\pm2.10}$
WIRE (Saragadam et al., 2023)	Wavelet	28.94 ± 0.21	28.20 ± 0.13	0.9912 ± 0.0005	31.27 ± 0.53	16.83 ± 1.85
NFSL (Saratchandran et al., 2024)	Sinusoidal	24.93 ± 0.07	$\overline{23.39\pm0.09}$	0.9925 ± 0.0001	38.92 ± 0.07	37.17 ± 2.88
Weight scaling (ours)	Sinusoidal	42.83 ± 0.35	42.03 ± 0.41	0.9941 ± 0.0002	$\overline{45.28 \pm 0.03}$	45.04 ± 3.23

We note that this behavior is in stark contrast with ReLU neural networks, where the weight scaling leads to a higher condition number, leading to a poor convergence (Chizat et al., 2019).

Kernel-task alignment. The kernel-task alignment—also known as the *energy concentration*—is the cumulative sum of the (normalized) dot products

$$\mathcal{E}(t) = \sum_{i:\lambda_i/\lambda_0 \ge t} (\phi_i^\top \mathbf{e})^2 / \|\mathbf{e}\|_2^2$$
(9)

where ϕ_i denotes the *i*-th eigenvector of the kernel and $\mathbf{e} = Y - f(X)$ denotes the vector of prediction errors in the pixels (Kopitkov & Indelman, 2020). This quantity measures how much of the residual signal is concentrated in the directions of large eigenvalues, which is theoretically easier to be expressed or optimized by kernel learning (Baratin et al., 2021; Yüce et al., 2022). In Fig. 5b, we compare the kernel-task alignments during the SNF training trajectories. We observe that the weight scaling gives a highly optimizable kernel throughout all stages of training.

5 EXPERIMENTS

In this section, we first address whether the weight scaling is effective in other data domains (Section 5.1); our answer is positive. Then, we discuss the factors that determine the optimal value of scaling factor α for the given target task (Section 5.2); we find that the optimal value does not depend much on the nature of each datum, but rather relies on the structural properties of the workload.

5.1 Main experiments

We validate the effectiveness of WS in different data domains by comparing against various neural fields. To compare the training speed, we fix the number of training steps and compare the training accuracy. In particular, we consider the following tasks and baselines.

Task: Image regression. The network is trained to approximate the signal intensity c, for each given normalized 2D pixel coordinates (x,y). For our experiments, we use Kodak (Kodak, 1999) and DIV2K (Agustsson & Timofte, 2017) datasets. Each image is resized to a resolution of 512×512 in grayscale, following Lindell et al. (2022); Seo et al. (2024). We report the training PSNR after a full-batch training for 150 iterations. For all NFs, we use five layers with width 512.

Task: Occupancy field. The network is trained to approximate the occupancy field of a 3D shape, *i.e.*, predict '1' for occupied coordinates and '0' for empty space. We use the voxel grid of size $512 \times 512 \times 512$ following Saragadam et al. (2023). For evaluation, we measure the training intersection-over-union (IoU) after 50 iterations on the 'Lucy' data from the 'Standard 3D Scanning Repository,' with the batch size 100k. We use NFs with five layers and width 256.

Task: Spherical data. We use 10 randomly selected samples from the ERA5 dataset, which contains temperature values corresponding to a grid of latitude ϕ and longitude θ , using the geographic coordinate system (GCS). Following Dupont et al. (2022), the network inputs are lifted to 3D coordinates, *i.e.*, transforming (ϕ, θ) to $(\cos(\phi) \cdot \cos(\theta), \cos(\phi) \cdot \sin(\theta), \sin(\phi))$. We report the training PSNR after 5k iterations of full-batch training. For NFs, we use five layers with width 256.

Task: Audio data. Audio is a 1D temporal signal, and the network is trained to approximate the amplitude of the audio at a given timestamp. We use the first 7 seconds of "Bach's Cello Suite No. 1," following Sitzmann et al. (2020b). We report the training PSNR after 1k iterations of full-batch training. For NFs, we use five layers with width 256.

Baselines. We compare the weight scaling against seven baselines; we have selected the memory-efficient and versatile neural fields, rather than highly specialized and heavy ones, such as Instant-NGP (Müller et al., 2022). More concretely, we use the following baselines: (1) *Xavier uniform*: the method by (Glorot & Bengio, 2010) applied on SNF, (2) *SIREN init*.: SNF using the standard initialization of SIREN (Sitzmann et al., 2020b), (3) *NFSL*: A recent initialization scheme motivated by scaling law (Saratchandran et al., 2024). (4) *ReLU+P.E.*: ReLU nets with positional encodings (Mildenhall et al., 2020). (5) *FFN*: Fourier feature networks Tancik et al. (2020). (6) *Gauss-Net*: MLP with Gaussian activations (Ramasinghe & Lucey, 2022). (7) *WIRE*: MLP with Gabor wavelet-based activations (Saragadam et al., 2023). The baselines (1-3) use SNFs as the backbone architecture, while (4-7) uses other architectures with different activation functions.

Other details. For selecting the hyperparameters for each NFs (including α), we have conducted a grid search. We use the Adam optimizer (Kingma, 2015) with a fixed learning rate specific to each data domain. Other experimental details are provided in Appendix E.

Result. Table 1 reports the comprehensive results across various data domains. We observe that the weight scaling significantly outperforms all baselines throughout all tasks considered. In Appendix E.4, we provide further qualitative results on various modalities, where we find that the weight scaling enhances capturing the high frequency details. These results support our hypothesis that the richer frequency spectrum provided by the weight scaling mitigates the spectral bias (Section 4.2), thereby enabling a faster training of neural fields.

Additional experiments. We have also conducted experiments on the NF-based dataset construction tasks (Papa et al., 2024). We report the results in Appendix E.2.

5.2 On selecting the optimal scaling factor

Now, we consider the problem of selecting an appropriate scaling factor without having to carefully tune it for each given datum. In particular, we are interested in finding the right α that maximizes the training speed yet incurs only negligible degradations in generalizability. More concretely, consider the task of Kodak image regression and seek to select the α that approximately solves

$$\label{eq:maximize} \underset{\alpha}{\text{maximize}} \quad \text{speed}(\alpha) \qquad \text{subject to} \quad \text{TestPSNR}(\alpha) \geq 0.95 \cdot \text{TestPSNR}(1). \tag{10}$$

where (again) the speed is the reciprocal of the number of steps required until the model meets the desired level of training loss, which we set to be the PSNR 50dB. Note that this optimization is similar to what has been discussed in Section 3.4.

In a nutshell, we observe in this subsection that this optimal scaling factor is largely driven by the structural properties of the optimization workload (such as model size and data resolution), and

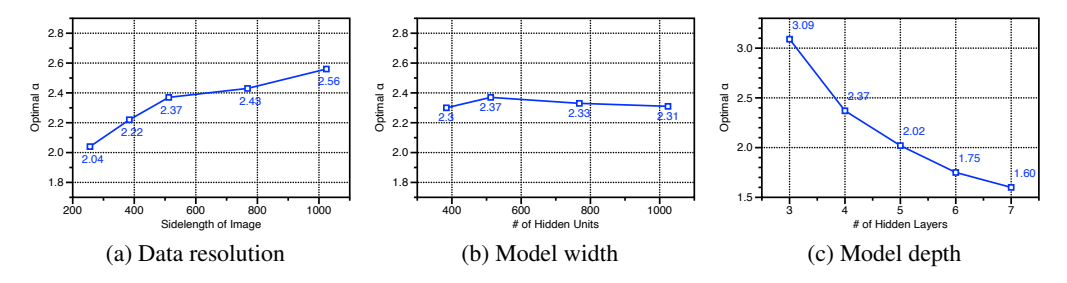


Figure 6. Optimal scaling factor vs. structural properties of the optimization workload. The data resolution, model width, and model depth have positive, no, and negative correlations with the optimal scaling factor.

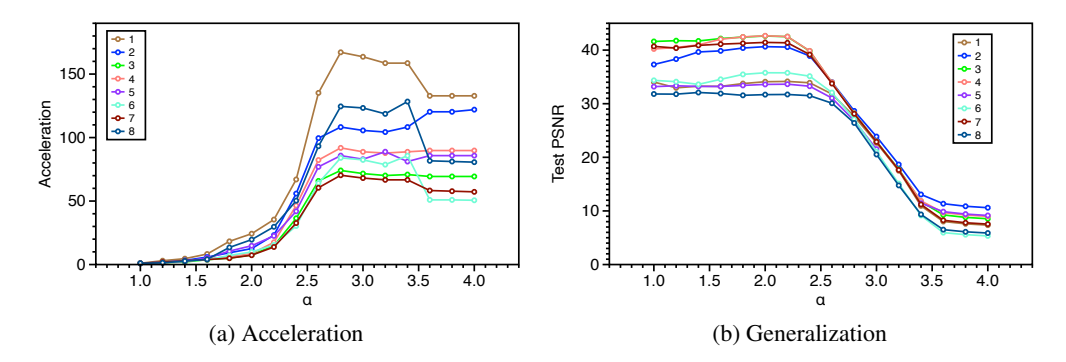


Figure 7. Scaling factor vs. the first 8 Kodak images. The behavior of each datum with respect to the scaling factor α is quite similar, in both acceleration and generalization performances.

remains relatively constant over the data. This suggests that the strategy of tuning α on a small number of data and transferring it to other data in the same datasets can be quite effective.

Structural properties. In Fig. 6, we visualize how changing the data resolution (512×512) by default), model width (512) by default), and model depth (4) by default) affects the value of optimal scaling factor. We observe that the higher data resolution and shallower model depth lead to a need for a higher scaling factor, with the width having very weak correlation. Commonly, we find that the resolution and depth are both intimately related to the frequency spectrum; higher resolution leads to a need for a higher frequency, and deeper networks can effectively utilize the relatively smaller scaling factors to represent high-frequency signals.

Data instances. In Fig. 7, we observe that both curves are strikingly quite similar in shape, having saturation and inflection points at the similar scaling factor. This may be due to the fact that natural images tend to exhibit a similar frequency distribution.

6 Conclusion

In this paper, we revisit the traditional initialization scheme of sinusoidal neural fields, and propose a new method called weight scaling, which scales the initialized weights by a specific factor. In practice, WS significantly accelerates the training speed of SNF across various data modalities, even outperforming recent neural field training methods. We have discovered that the difference between the traditional and WS initialization comes from both the change in the frequency spectrum of the initial functional and the change in the layerwise learning rates, where the former plays a more crucial role in acceleration. Through extensive theoretical and empirical analyses, we have revealed that the WS positively impacts the learning dynamics by maintaining a well-conditioned optimization path throughout the training process.

Limitations and future direction. The limitations of our work lie in the fact that the analysis has been conducted for only neural fields using sinusoidal activation functions, rather than general neural field architectures; whether the weight scaling is effective on other architectures remains an open question. Also, from a theoretical perspective, our analyses does not provide a definitive answer on the acceleration mechanisms, lacking an explicit convergence bound. As a final remark,

our work is closely related to the *implicit bias of initialization scale* (Azulay et al., 2021), which is an emerging topic in understanding the mechanics of neural network training. However, there remains a significant gap between theory and practice in this area, as the current interpretation is limited to shallow, homogeneous, and linear networks (Varre et al., 2023; Kunin et al., 2024), rather than general nonlinear networks. The next step is to understand the implicit bias in networks with general activation functions, where the scale of initialization is not necessarily equivalent to output scaling. We leave this as future work.

REPRODUCIBILITY STATEMENT

Most experiments in our work are based on widely used neural field baselines, whose official source codes are publicly available online. The only new part, *i.e.*, our proposed algorithm, is rather simple and only requires multiplying constants to the initial weights. While the implementation is quite simple, we will also release our code for our algorithm and the experiments as a public repository, upon the preparation of the camera-ready version of the paper.

REFERENCES

- Eirikur Agustsson and Radu Timofte. NTIRE 2017 challenge on single image super-resolution: Dataset and study. In *The IEEE Conference on Computer Vision and Pattern Recognition (CVPR) Workshops*, 2017.
- Shahar Azulay, Edward Moroshko, Mor Shpigel Nacson, Blake E Woodworth, Nathan Srebro, Amir Globerson, and Daniel Soudry. On the implicit bias of initialization shape: Beyond infinitesimal mirror descent. In *International Conference on Machine Learning*, 2021.
- Aristide Baratin, Thomas George, César Laurent, R Devon Hjelm, Guillaume Lajoie, Pascal Vincent, and Simon Lacoste-Julien. Implicit regularization via neural feature alignment. In *International Conference on Artificial Intelligence and Statistics*, 2021.
- Ronen Basri, Meirav Galun, Amnon Geifman, David Jacobs, Yoni Kasten, and Shira Kritchman. Frequency bias in neural networks for input of non-uniform density. In *International Conference on Machine Learning*, 2020.
- Shannon R Bowling, Mohammad T Khasawneh, Sittichai Kaewkuekool, and Byung Rae Cho. A logistic approximation to the cumulative normal distribution. *Journal of Industrial Engineering and Management*, 2009.
- Yinbo Chen and Xiaolong Wang. Transformers as meta-learners for implicit neural representations. In *European Conference on Computer Vision*, 2022.
- Lenaic Chizat, Edouard Oyallon, and Francis Bach. On lazy training in differentiable programming. In *Advances in Neural Information Processing Systems*, 2019.
- Emilien Dupont, Hrushikesh Loya, Milad Alizadeh, Adam Golinski, Yee Whye Teh, and Arnaud Doucet. COIN++: Neural compression across modalities. *Transactions on Machine Learning Research*, 2022.
- Behrooz Ghorbani, Shankar Krishnan, and Ying Xiao. An investigation into neural net optimization via Hessian eigenvalue density. In *International Conference on Machine Learning*, 2019.
- Xavier Glorot and Yoshua Bengio. Understanding the difficulty of training deep feedforward neural networks. In *International Conference on Artificial Intelligence and Statistics*, 2010.
- Daniele Grattarola and Pierre Vandergheynst. Generalised implicit neural representations. In *Advances in Neural Information Processing Systems*, 2022.
- Zongyu Guo, Gergely Flamich, Jiajun He, Zhibo Chen, and José Miguel Hernández-Lobato. Compression with Bayesian implicit neural representations. In *Advances in Neural Information Processing Systems*, 2023.
- Kaiming He, Xiangyu Zhang, Shaoqing Ren, and Jian Sun. Delving deep into rectifiers: Surpassing human-level performance on ImageNet classification. In *Proceedings of the IEEE/CVF International Conference on Computer Vision*, 2015.
- Evangelos K. Ifantis and Panayiotis D. Siafarikas. Inequalities involving Bessel and modified Bessel functions. *Journal of mathematical analysis and applications*, 1990.
- Arthur Jacot, Franck Gabriel, and Clément Hongler. Neural tangent kernel: Convergence and generalization in neural networks. In *Advances in Neural Information Processing Systems*, 2018.

- Hyomin Kim, Yunhui Jang, Jaeho Lee, and Sungsoo Ahn. Hybrid neural representations for spherical data. In *International Conference on Machine Learning*, 2024.
- Diederik P Kingma. Adam: A method for stochastic optimization. In *International Conference on Learning Representations*, 2015.
- E. Kodak. Kodak dataset, 1999. URL https://r0k.us/graphics/kodak/.
- Dmitry Kopitkov and Vadim Indelman. Neural spectrum alignment: Empirical study. In *Artificial Neural Networks and Machine Learning*, 2020.
- Daniel Kunin, Allan Raventós, Clémentine Dominé, Feng Chen, David Klindt, Andrew Saxe, and Surya Ganguli. Get rich quick: Exact solutions reveal how unbalanced initializations promote rapid feature learning. *arXiv preprint arXiv:2406.06158*, 2024.
- Jaeho Lee, Jihoon Tack, Namhoon Lee, and Jinwoo Shin. Meta-learning sparse implicit neural representations. In *Advances in Neural Information Processing Systems*, 2021.
- David B. Lindell, Dave Van Veen, Jeong Joon Park, and Gordon Wetzstein. BACON: Band-limited coordinate networks for multiscale scene representation. In *Proceedings of the IEEE/CVF Conference on Computer Vision and Pattern Recognition*, 2022.
- Zhen Liu, Hao Zhu, Qi Zhang, Jingde Fu, Weibing Deng, Zhan Ma, Yanwen Guo, and Xun Cao. FINER: Flexible spectral-bias tuning in implicit neural representation by variable-periodic activation functions. In *Proceedings of the IEEE/CVF Conference on Computer Vision and Pattern Recognition*, 2024.
- Qi Ma, Danda Pani Paudel, Ender Konukoglu, and Luc Van Gool. Implicit-Zoo: A large-scale dataset of neural implicit functions for 2D images and 3D scenes. *arXiv preprint arXiv:2406.17438*, 2024.
- Harsh Mehta, Ashok Cutkosky, and Behnam Neyshabur. Extreme memorization via scale of initialization. In *International Conference on Learning Representations*, 2021.
- Ben Mildenhall, Pratul P Srinivasan, Matthew Tancik, Jonathan T Barron, Ravi Ramamoorthi, and Ren Ng. NeRF: Representing scenes as neural radiance fields for view synthesis. In *European Conference on Computer Vision*, 2020.
- Thomas Müller, Alex Evans, Christoph Schied, and Alexander Keller. Instant neural graphics primitives with a multiresolution hash encoding. *ACM transactions on graphics (TOG)*, 2022.
- Roman Novak, Lechao Xiao, Jiri Hron, Jaehoon Lee, Alexander A. Alemi, Jascha Sohl-Dickstein, and Samuel S. Schoenholz. Neural tangents: Fast and easy infinite neural networks in Python. In *International Conference on Learning Representations*, 2020.
- Guillermo Ortiz-Jiménez, Seyed-Mohsen Moosavi-Dezfooli, and Pascal Frossard. What can linearized neural networks actually say about generalization? In *Advances in Neural Information Processing Systems*, 2021.
- Sourav Pal, Harshavardhan Adepu, Clinton Wang, Polina Golland, and Vikas Singh. Implicit representations via operator learning. In *International Conference on Machine Learning*, 2024.
- Samuele Papa, Riccardo Valperga, David Knigge, Miltiadis Kofinas, Phillip Lippe, Jan-Jakob Sonke, and Efstratios Gavves. How to train neural field representations: A comprehensive study and benchmark. In *Proceedings of the IEEE/CVF Conference on Computer Vision and Pattern Recognition*, 2024.
- Ben Poole, Ajay Jain, Jonathan T. Barron, and Ben Mildenhall. DreamFusion: Text-to-3D using 2D diffusion. In *International Conference on Learning Representations*, 2023.
- Nasim Rahaman, Aristide Baratin, Devansh Arpit, Felix Draxler, Min Lin, Fred Hamprecht, Yoshua Bengio, and Aaron Courville. On the spectral bias of neural networks. In *International Conference on Machine Learning*, 2019.

- Sameera Ramasinghe and Simon Lucey. Beyond periodicity: Towards a unifying framework for activations in coordinate-MLPs. In *European Conference on Computer Vision*, 2022.
- Daniel Rebain, Soroosh Yazdani, Kwang Moo Yi, and Andrea Tagliasacchi. Neural fields as distributions: Signal processing beyond Euclidean space. In *Proceedings of the IEEE/CVF Conference on Computer Vision and Pattern Recognition*, 2024.
- Basri Ronen, David Jacobs, Yoni Kasten, and Shira Kritchman. The convergence rate of neural networks for learned functions of different frequencies. In *Advances in Neural Information Processing Systems*, 2019.
- Marc Rußwurm, Konstantin Klemmer, Esther Rolf, Robin Zbinden, and Devis Tuia. Geographic location encoding with spherical harmonics and sinusoidal representation networks. In *International Conference on Learning Representations*, 2024.
- Vishwanath Saragadam, Daniel LeJeune, Jasper Tan, Guha Balakrishnan, Ashok Veeraraghavan, and Richard G Baraniuk. WIRE: Wavelet implicit neural representations. In *Proceedings of the IEEE/CVF Conference on Computer Vision and Pattern Recognition*, 2023.
- Hemanth Saratchandran, Sameera Ramasinghe, and Simon Lucey. From activation to initialization: Scaling insights for optimizing neural fields. In *Proceedings of the IEEE/CVF Conference on Computer Vision and Pattern Recognition*, 2024.
- Jonathan Richard Schwarz, Jihoon Tack, Yee Whye Teh, Jaeho Lee, and Jinwoo Shin. Modality-agnostic variational compression of implicit neural representations. In *International Conference on Machine Learning*, 2023.
- Junwon Seo, Sangyoon Lee, Kwang In Kim, and Jaeho Lee. In search of a data transformation that accelerates neural field training. In *Proceedings of the IEEE/CVF Conference on Computer Vision and Pattern Recognition*, 2024.
- Louis Serrano, Lise Le Boudec, Armand Kassaï Koupaï, Thomas X Wang, Yuan Yin, Jean-Noël Vittaut, and Patrick Gallinari. Operator learning with neural fields: Tackling PDEs on general geometries. In *Advances in Neural Information Processing Systems*, 2023.
- Zenglin Shi, Pascal Mettes, Subhransu Maji, and Cees G M Snoek. On measuring and controlling the spectral bias of the deep image prior. *International Journal of Computer Vision*, 2022.
- Anthony Simeonov, Yilun Du, Andrea Tagliasacchi, Joshua B Tenenbaum, Alberto Rodriguez, Pulkit Agrawal, and Vincent Sitzmann. Neural descriptor fields: SE(3)-equivariant object representations for manipulation. In *International Conference on Robotics and Automation*, 2022.
- Vincent Sitzmann, Michael Zollhöfer, and Gordon Wetzstein. Scene representation networks: Continuous 3D-structure-aware neural scene representations. In *Advances in Neural Information Processing Systems*, 2019.
- Vincent Sitzmann, Eric R. Chan, Richard Tucker, Noah Snavely, and Gordon Wetzstein. MetaSDF: Meta-learning signed distance functions. In Advances in Neural Information Processing Systems, 2020a.
- Vincent Sitzmann, Julien Martel, Alexander Bergman, David Lindell, and Gordon Wetzstein. Implicit neural representations with periodic activation functions. In *Advances in Neural Information Processing Systems*, 2020b.
- Matthew Tancik, Pratul Srinivasan, Ben Mildenhall, Sara Fridovich-Keil, Nithin Raghavan, Utkarsh Singhal, Ravi Ramamoorthi, Jonathan Barron, and Ren Ng. Fourier features let networks learn high frequency functions in low dimensional domains. In *Advances in Neural Information Processing Systems*, 2020.
- Matthew Tancik, Ben Mildenhall, Terrance Wang, Divi Schmidt, Pratul P. Srinivasan, Jonathan T. Barron, and Ren Ng. Learned initializations for optimizing coordinate-based neural representations. In *Proceedings of the IEEE/CVF Conference on Computer Vision and Pattern Recognition*, 2021.

- Gal Vardi. On the implicit bias in deep-learning algorithms. Communications of the ACM, 2023.
- Aditya Vardhan Varre, Maria-Luiza Vladarean, Loucas Pillaud-Vivien, and Nicolas Flammarion. On the spectral bias of two-layer linear networks. In *Advances in Neural Information Processing Systems*, 2023.
- Sifan Wang, Hanwen Wang, and Paris Perdikaris. On the eigenvector bias of Fourier feature networks: From regression to solving multi-scale PDEs with physics-informed neural networks. *Computer Methods in Applied Mechanics and Engineering*, 2021.
- Blake Woodworth, Suriya Gunasekar, Jason D Lee, Edward Moroshko, Pedro Savarese, Itay Golan, Daniel Soudry, and Nathan Srebro. Kernel and rich regimes in overparametrized models. In *Conference on Learning Theory*, 2020.
- Lechao Xiao, Yasaman Bahri, Jascha Sohl-Dickstein, Samuel S. Schoenholz, and Jeffrey Pennington. Dynamical isometry and a mean field theory of cnns: How to train 10,000-layer vanilla convolutional neural networks. In *International Conference on Machine Learning*, 2018.
- Yiheng Xie, Towaki Takikawa, Shunsuke Saito, Or Litany, Shiqin Yan, Numair Khan, Federico Tombari, James Tompkin, Vincent Sitzmann, and Srinath Sridhar. Neural fields in visual computing and beyond. In *Computer Graphics Forum*, 2022.
- Zhi-Qin John Xu, Yaoyu Zhang, Tao Luo, Yanyang Xiao, and Zheng Ma. Frequency principle: Fourier analysis sheds light on deep neural networks. *Communications in Computational Physics*, 2020.
- Zhewei Yao, Amir Gholami, Kurt Keutzer, and Michael W Mahoney. PyHessian: Neural networks through the lens of the Hessian. In *IEEE international conference on big data*, 2020.
- Gizem Yüce, Guillermo Ortiz-Jiménez, Beril Besbinar, and Pascal Frossard. A structured dictionary perspective on implicit neural representations. In *Proceedings of the IEEE/CVF Conference on Computer Vision and Pattern Recognition*, 2022.
- Hongyi Zhang, Yann N Dauphin, and Tengyu Ma. Fixup initialization: Residual learning without normalization. In *International Conference on Learning Representations*, 2019.

Appendix

A	Deta	niled statement and the derivation of Proposition 3.1	17
	A.1	Proof of Lemma A.1	17
	A.2	Proof of Lemma A.2	17
В	Proc	ofs in Section 4	21
	B.1	Proof of Lemma 4.1	21
	B.2	Proof of Lemma 4.2	21
	B.3	Details of Section 4.1	21
C	Deta	nils of NTK Analysis and beyond	23
	C.1	Preliminaries	23
	C.2	Kernel regression with gradient flow	23
	C.3	Non-kernel approach: analysis via Hessian eigenvalues	25
D	Freq	quency spectrum of 2D images	26
E	Exp	erimental details and qualitative results	27
	E.1	Training settings and baselines	27
	E.2	Neural dataset experiements	28
	E.3	Training for additional iterations	28
	F.4	Qualitative results	29

A DETAILED STATEMENT AND THE DERIVATION OF PROPOSITION 3.1

In this section, we provide a more detailed statement and derivation of Proposition 3.1, where we have extended the distribution-preserving claims of Sitzmann et al. (2020b) on $\alpha = 1$ to the cases of $\alpha \ge 1$, thus covering the initialization with weight scaling.

We note that we generally follow the approach of Sitzmann et al. (2020b) in terms of the formalisms; we provide rough approximation guarantees (Lemmas A.1 and A.2), one of which relies on a numerical analysis of a function that is difficult to be expressed in a closed form (Lemma A.2).

In particular, we are concerned with showing the following two points:

- Activations to pre-activations. We show that, for $\alpha \geq 1$, the pre-activation of a layer with weight-scaled uniform activations and arcsin input distributions are approximately distributed as a Gaussian distribution with variance scaled by α (Lemma A.1).
- **Pre-activations to activations.** Then, we show that, for $\alpha \geq 1$, post-activation distribution of the Gaussian distribution with α -scaled variance is distributed as an arcsin distribution (Lemma A.2).

More formally, our lemma are as follows.

Lemma A.1 (Arcsin to Gaussian distributions). Let the weights W_l of the l-th layer be sampled i.i.d. from $\operatorname{Unif}(-c/\sqrt{n}, c/\sqrt{n})$, and the activation of the (l-1)-th layer Z_{l-1} follow the i.i.d. $\operatorname{arcsin}(-1,1)$. Then, the distribution of the pre-activation of the l-th layer Y_l converges in distribution to a Gaussian distribution $\mathcal{N}(0,c^2/6)$ as the number of hidden units n tends to infinity.

Lemma A.2 (Gaussian to arcsin distributions, with numerical proof). Let the pre-activation distribution X has a Gaussian distribution $\mathcal{N}(0, \alpha^2)$ for some $\alpha \geq 1$. Then the activation distribution $Y = \sin(X)$ is distributed as $\arcsin(-1, 1)$.

Note that, by plugging in $c = \alpha \sqrt{6}$ to the Lemma A.1 as in the proposed weight scaling, we get the normal distribution $\mathcal{N}(0, \alpha^2)$ as an output distribution.

We provide the proofs of these lemma in Appendices A.1 and A.2, respectively. For all derivations, we simply ignore the issue of the frequency scaling term ω_0 , and simply let it equal to 1.

A.1 PROOF OF LEMMA A.1

For simplicity, let us denote a pre-activation of a neuron in the lth layer by y. Let the weight vector connected to this output neuron as $\mathbf{w} \in \mathbb{R}^n$, with each entries drawn independently from $\mathrm{Unif}(-c/\sqrt{n},c/\sqrt{n})$. Also, let the corresponding input activation from the (l-1)th layer be denoted by $\mathbf{z} \in \mathbb{R}^n$, with each entry drawn independently from $\arcsin(-1,1)$. Now, it suffices to show that $y = \mathbf{w}^{\top}\mathbf{z}$ converges in distribution to $\mathcal{N}(0,c^2/6)$ as n goes to infinity.

To show this point, we simply invoke the central limit theorem for the i.i.d. case. For CLT to hold, we only need to check that each summand $(w_i z_i)$ of the dot product $\mathbf{w}^\top \mathbf{z} = \sum w_i z_i$ has a finite mean and variance.

$$\mathbf{w}^{\top}\mathbf{z} = \sum_{i=1}^{d} w_i z_i \tag{11}$$

has a finite mean and variance $\mathbf{w}^{\top}\mathbf{z}$ has a zero mean and a finite variance. We know that $\mathbb{E}[w_i z_i] = 0$, as two random variables are independent and $\mathbb{E}[w_i] = 0$. To show that the variance is finite, we can proceed as

$$Var(w_i z_i) = Var(w_i)Var(z_i) = \frac{c^2}{3n} \frac{1}{2} = \frac{c^2}{6n},$$
 (12)

where the first equality holds as each variables are independent and zero-mean. Summing over n indices, we get what we want.

A.2 PROOF OF LEMMA A.2

By the 3σ rule, 99.7% of the mass of the Gaussian distribution $\mathcal{N}(0,\alpha^2)$ lies within the finite support $[-3\alpha,3\alpha]$. The CDF of Y can be written as

$$F_Y(y) = P(Y \le y) = P(\sin(X) \le y). \tag{13}$$

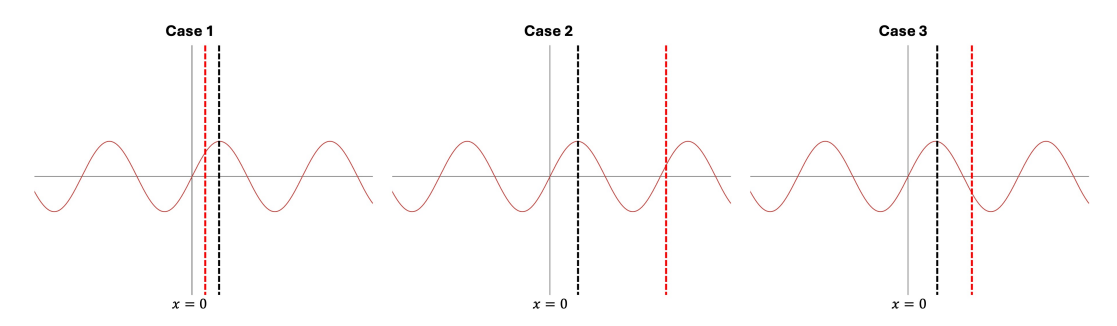


Figure 8. Visualization of the cases in Lemma A.2. In $y = \sin(x)$, Red line: $x = 3\alpha$ and Black line: $x = \frac{\pi}{2}$

Different from the settings of Sitzmann et al. (2020b), the sinusoidal activation is not a bijection in general within the support $[-3\alpha, 3\alpha]$, *i.e.*, not directly invertible. Thus, we break it down into three cases (Fig. 8): Case 1, where the endpoint 3α is less than $\pi/2$, Case 2, where 3α is in the increasing region of $\sin(\cdot)$, and Case 3, where 3α is in the decreasing region. We study each case:

Case 1 ($\alpha < \pi/6$). Here, we have

$$F_Y(y) = P(X \le \arcsin y) = F_X(\arcsin y) \approx \frac{1}{2} + \frac{1}{2} \tanh\left(\frac{\beta}{\alpha}\arcsin y\right),$$
 (14)

where the last approximation invokes the Gaussian CDF approximation (Bowling et al., 2009). In this case, the CDF of Y does not approximate the CDF of $\arcsin(-1,1)$. That is, the second-order derivative of F decreases in [-1,0] and increases in [0,1], while the CDF of the arcsin distribution behaves in an opposite way.

Now, suppose that α is sufficiently large ($\alpha \geq \pi/6$), *i.e.*, <u>case 2</u> or <u>case 3</u>. Here, we will consider the nearest peak/valley that falls outside the $[-3\alpha, 3\alpha]$ interval. More concretely, let γ be defined as the period index of such peak/valley, i.e.,

$$\gamma = \min\{\gamma_1, \gamma_2\}, \quad \text{where}$$
 (15)

$$\gamma_1 = \min \left\{ n \in \mathbb{N} \mid \frac{(4n+1)\pi}{2} \ge 3\alpha \cap \sin \left(\frac{(4n+1)\pi}{2} \right) = +1 \right\}$$
 (peak; case 2) (16)

$$\gamma_2 = \min\left\{n \in \mathbb{N} \mid \frac{(4n-1)\pi}{2} \ge 3\alpha \cap \sin\left(\frac{(4n-1)\pi}{2}\right) = -1\right\} \quad \text{(valley; case 3)} \quad (17)$$

By considering the range up until such peaks/valleys, we can ensure that the probability of X lying within this range is greater than 0.997.

Now, let's proceed to analyze the case 2; the case 3 can be handled similarly.

Case 2. We break down the CDF of Y as

$$F_Y(y) = F_{Y,\text{center}}(y) + F_{Y,\text{inc}}(y) + F_{Y,\text{dec}}(y). \tag{18}$$

Here, $F_{Y,\text{center}}(y)$ denotes the CDF of the bijective region, i.e., $x \in [-\pi/2, \pi/2]$, and $F_{Y,\text{inc}}(y)$ denotes the region where the $\sin(\cdot)$ is increasing and $F_{Y,\text{dec}}(y)$ denotes where $\sin(\cdot)$ is decreasing. Then, each of these components can be written as:

$$F_{Y,\text{center}}(y) = P(-\pi/2 \le X \le \arcsin y) = F_X(\arcsin y) - F_X(-\pi/2)$$
(19)

$$F_{Y,\text{inc}}(y) = \sum_{n=1}^{\gamma_1} \left[F_X(\arcsin y + 4n\pi/2) - F_X((4n-1)\pi/2) \right]$$

+
$$F_X(\arcsin y - 4n\pi/2) - F_X(-(4n+1)\pi/2)$$
 (20)

$$F_{Y,\text{dec}}(y) = \sum_{n=1}^{\gamma_1} \left[F_X((4n-1)\pi/2) - F_X(-\arcsin y + (4n-2)\pi/2) + F_X(-(4n-3)\pi/2) - F_X(-\arcsin y - (4n-2)\pi/2) \right]$$
(21)

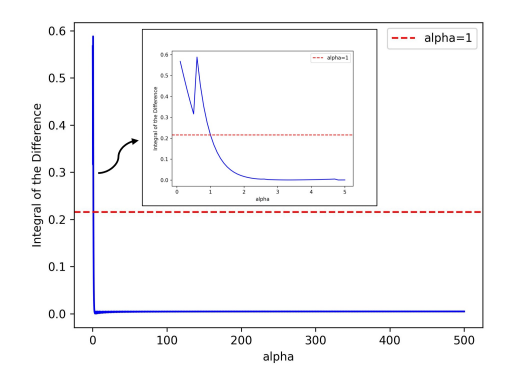


Figure 9. Approximated CDF with increasing in α . Red line indicates the reference error. When α goes larger, the error converges to limit near zero.

Combining these terms, we get:

$$F_Y(y) = F_X \left(\arcsin y\right) - F_X \left(-\pi/2\right)$$

$$+ \sum_{n=1}^{\gamma_1} \left[F_X(-(4n-3)\pi/2) - F_X(-(4n+1)\pi/2) + F_X(\arcsin y + 4n\pi/2) + F_X(\arcsin y - 4n\pi/2) - F_X(-\arcsin y + (4n-2)\pi/2) - F_X(-\arcsin y - (4n-2)\pi/2) \right]$$
(22)

Using the logistic approximation and Taylor's first-order expansion at $z = \arcsin y = 0$, i.e., $f(z) \approx \frac{f'(z)}{11}(z-0) + f(0)$, this can be further approximated by

$$F_Y(y) = \left[\frac{\beta}{2\alpha} h'(0) + \sum_{n=1}^{\gamma_1} \left(\frac{\beta}{\alpha} \left(h' \left(\frac{4n\beta\pi}{2\alpha} \right) + h' \left(\frac{(4n-2)\beta\pi}{2\alpha} \right) \right) \right) \right] z$$

$$- \frac{1}{2} h \left(-\frac{\beta\pi}{2\alpha} \right) + \sum_{n=1}^{\gamma_1} \left[\frac{1}{2} h \left(-\frac{(4n-3)\beta\pi}{2\alpha} \right) - \frac{1}{2} h \left(-\frac{(4n+1)\beta\pi}{2\alpha} \right) \right], \tag{23}$$

where h is the tanh function. The above equation has variables γ_1 and α . Thus, we can rewrite it as:

$$F_Y(y) = f(\alpha) \cdot \arcsin y + g(\alpha),$$
 (24)

$$f(\alpha) = \frac{\beta}{2\alpha}h'(0) + \frac{\beta}{\alpha}\sum_{n=1}^{\gamma_1} \left[h'\left(\frac{4n\beta\pi}{2\alpha}\right) + h'\left(\frac{(4n-2)\beta\pi}{2\alpha}\right)\right],\tag{25}$$

$$g(\alpha) = -\frac{1}{2}h\left(-\frac{\beta\pi}{2\alpha}\right) + \frac{1}{2}\sum_{n=1}^{\gamma_1} \left[h\left(-\frac{(4n-3)\beta\pi}{2\alpha}\right) - h\left(-\frac{(4n+1)\beta\pi}{2\alpha}\right)\right]. \tag{26}$$

Now, we compare the $F_X(x)$ to ground truth CDF of $\arcsin(-1,1)$, i.e., $\frac{2}{\pi}\arcsin\sqrt{\frac{x+1}{2}}$. As the closed form solution is not obtainable, we numerically compute the difference in integration over input domain:

$$\hat{\alpha} \in \left\{ \alpha \left| \int_{-1}^{1} \left| F_X(x, \alpha) - \frac{2}{\pi} \arcsin\left(\sqrt{\frac{x+1}{2}}\right) \right| dx \right\}$$
 (27)

$$\leq \int_{-1}^{1} \left| F_X(x,1) - \frac{2}{\pi} \arcsin\left(\sqrt{\frac{x+1}{2}}\right) \right| dx \right\}. \tag{28}$$

This indicates that the RHS term represents the cumulative error from the default initialization, which is assumed to be valid for preserving the forward signal. If the LHS is smaller than the RHS for some value of $\hat{\alpha}$ that satisfies the inequality, it intuitively follows that the elements in $\hat{\alpha}$ provide a valid scale. In Fig. 9, we empirically demonstrate that as the scaling factor α increases, the error between the ground truth and the approximated CDF decreases with some limit near zero, which implies $\hat{\alpha} \in [1, \infty)$.

B Proofs in Section 4

B.1 Proof of Lemma 4.1

To formally prove this lemma, we first bring the generalized form from Yüce et al. (2022).

Lemma B.1 (From Yüce et al. (2022, Appendix A.2)). Suppose that the model can be written as $f(x) = W^{(3)} \sin(W^{(2)} \sin(W^{(1)}x))$, where $W^{(1)} \in \mathbb{R}^{d_1}$, $W^{(2)} \in \mathbb{R}^{d_2 \times d_1}$, and $W^{(3)} \in \mathbb{R}^{1 \times d_2}$. Then, the model can be equivalently written as:

$$f(x) = \sum_{m=0}^{d_2-1} \sum_{i_1,\dots,i_{d_1}=-\infty}^{\infty} \left(\prod_{k=0}^{d_1-1} J_k \left(w_k^{(2)} \right) \right) w_m^{(3)} \sin \left(\left(\sum_{k=0}^{d_1-1} i_k \cdot w_k^{(1)} \right) x \right), \tag{29}$$

where the lowercase $w_k^{(i)}$ denotes the k-th column of the matrix $W^{(i)}$.

We specialize this lemma to the case of width-one SNF, i.e., $d_1 = d_2 = 1$. We proceed as

$$f(x) = W^{(3)}\sin(W^{(2)}\sin(W^{(1)}x))$$
(30)

$$=2\sum_{k=0}^{\infty}J_{2k+1}(W^{(2)})\sin((2k+1)W^{(1)}x),\tag{31}$$

where the second equality is due to the Jacobi-Anger identity. By restricting the sum to $l \in \mathbb{Z}_{\text{odd}}$, we can further simplify as

$$f(x; \mathbf{W}) = 2 \sum_{\ell \in \mathbb{Z}_{\text{odd}}} J_{\ell}(W^{(2)}) \sin(\ell W^{(1)} x).$$
 (32)

B.2 Proof of Lemma 4.2

For notational simplicity, we denote $x := W^{(2)}$.

First, we note that the first root of the ℓ th order Bessel function, denoted by $j_{\ell,1}$, satisfies the inequality $j_{\ell,1} > \pi/2$ for all $\ell \in \mathbb{N}$. Next, recall the results of Ifantis & Siafarikas (1990) that

$$\frac{x}{2(\ell+1)} < \frac{J_{\ell+1}(x)}{J_{\ell}(x)} < \frac{x}{2\ell+1}, \qquad \forall x \in (0, \pi/2).$$
 (33)

Similarly, for $J_{\ell+2}(x)$, we have

$$\frac{x}{2(\ell+2)} < \frac{J_{\ell+2}(x)}{J_{\ell+1}(x)} < \frac{x}{2\ell+3}, \qquad \forall x \in (0, \pi/2). \tag{34}$$

Multiplying two inequalities, we get the desired claim.

B.3 Details of Section 4.1

In this subsection, we provide more precise details of gradient bound of SNFs, with simple L-layer, 1-width network. Note that the bound can be generalized to arbitrary width, with matrix product computation.

Let L-layer simple SNF, f(x), as in the main paper:

$$f(x) = W^{(L)}\sin(W^{(L-1)}\sin(\cdots\sin(W^{(1)}x)\cdots)). \tag{35}$$

The network is trained with MSE loss function with gradient-based method, then the gradient of weight of each layer is computed as:

$$\frac{\partial L}{\partial W^{(k)}} = \frac{\partial L}{\partial f} \cdot \frac{\partial f}{\partial W^{(k)}} = R_0 \cdot \frac{\partial f}{\partial W^{(k)}}, \quad \text{for} \quad k \in [1, L], \tag{36}$$

where R_0 denotes the initial residual, i.e., $f(x) - Y_{\text{true}}$. We additionally assume that R_0 is independent from various initalizations techniques. Then, $\partial f/\partial W^{(k)}$ only effects to gradients. By

the simple property of sine function: $\max_x \sin(x) = \max_x (d\sin(x)/dx) = 1$, the gradients are bounded with:

$$\left| \frac{\partial L}{\partial W^{(k)}} \right| = R_{t=0} \prod_{m=1}^{L-k} \left(\mathbb{1}_{L>k} W^{(L-m+1)} \cdot G_k(x) \cdot x^{L-k-1} + \mathbb{1}_{L=k} G_k(x) \right)$$
(37)

$$\leq R_{t=0} \prod_{m=1}^{L-k} \left(\mathbb{1}_{L>k} W^{(L-m+1)} \cdot \max_{x} G_k(x) \cdot x^{L-k-1} + \mathbb{1}_{L=k} \max_{x} G_k(x) \right)$$
(38)

$$= R_{t=0} \prod_{m=1}^{L-k} \left(\mathbb{1}_{L>k} W^{(L-m+1)} \cdot x^{L-k-1} + \mathbb{1}_{L=k} \right)$$
(39)

$$\leq R_{t=0} \prod_{m=1}^{L-k} \left(\mathbb{1}_{L>k} W^{(L-m+1)} + \mathbb{1}_{L=k} \right),$$
(40)

where $G_k(x)$ denotes a composite sinusoidal function from the gradient derivation process and 1 is a indicator function. Since the maximum value of a composite sinusoidal function is always equal to or less than $1, |G_k(x)|$ is bounded by 1. Note that Eq. (40) is satisfied due to the bounds on input domain, i.e., $x \in [-1, 1]$.

C DETAILS OF NTK ANALYSIS AND BEYOND

C.1 PRELIMINARIES

The Neural Tangent Kernel (NTK) framework views neural networks as kernel machines, where the kernel is defined as the dot-product of the gradients from two different data point (Jacot et al., 2018). In other words, each element of NTK can be expressed as $K(x_i, x_j) = \langle \nabla_{\mathbf{W}} f(x_i), \nabla_{\mathbf{W}} f(x_j) \rangle$. Assuming an infinitely wide network trained with an infinitesimally small learning rate (i.e., gradient flow) and using a specific parameterization (i.e., NTK parameterization), the NTK converges to a deterministic kernel that does not evolve during training. However, in practice, neural networks are composed of finite-width layers, which introduces challenges for analysis using NTK-style theory. In this context, we study the empirical Neural Tangent Kernel (eNTK), where we do not require the assumption of a stationary kernel. Recent researches (Kopitkov & Indelman, 2020; Ortiz-Jiménez et al., 2021; Baratin et al., 2021) show that, with eNTKs non-linearly evolve during training, this kernel can serve as a measure of the difficulty of learning a particular task.

C.2 KERNEL REGRESSION WITH GRADIENT FLOW

First, we provide a well-founded spectral analysis of NTK regression. Assuming the network is trained with a constant training set X and their label set Y (i.e., $((x_1, y_1), \dots, (x_N, y_N))$), $x, y \in \mathbb{R}$), where $f(X; W_t) = f(W_t)$, and the loss function L is defined as MSE. We can then express the time-dependent dynamics of the function using the NTK. To begin, we start with the equation for vanilla GD:

$$W_{t+1} = W_t - \eta \nabla_W L(W_k) \tag{41}$$

$$\frac{W_{t+1} - W_t}{\eta} = -\nabla_W L(W_k). \tag{42}$$

With infinitesimally small learning rate, i.e., gradient flow, then:

$$\frac{dW_t}{dt} = -\nabla_W L(W_t)$$

$$= -\nabla_W f(W_t) \cdot (f(W_t) - Y_{\text{true}}).$$
(43)

Eq. 43 indicates the dynamics of the weights. Using a simple chain rule, we can modify the equation to represent the dynamics of the function, with the definition of NTK (i.e., $K_t \in \mathbb{R}^{N \times N}$):

$$\frac{df(W_t)}{dt} = \frac{df(W_t)}{dW_t} \cdot \frac{dW_t}{dt} = -\langle \nabla_W f(W_t), \nabla_W f(W_t) \rangle (f(W_t) - Y_{\text{true}})$$

$$= -K_t \cdot (f(W_t) - Y_{\text{true}}). \tag{44}$$

Note that the element-wise representation of NTK is can be written as $K_t(x_i, x_j) = \langle \nabla_W f(x_i, W_t), \nabla_W f(x_j, W_t) \rangle \in \mathbb{R}$, where x_k denotes k-th data point in the entire training set X. Now, let $g(W_t) := f(W_t) - Y_{\text{true}}$, then Eq. 44 can be rewritten as:

$$\frac{dg(W_t)}{dt} = -K_t \cdot g(W_t). \tag{45}$$

Eq. 45 is a simple ordinary differential equation (ODE) and can be solved in the form of exponential growth by assuming the NTK is constant during update; $K_t = K_0$:

$$q(W_t) = e^{-t \cdot K_t} \cdot q(W_0) \tag{46}$$

$$f(W_t) - Y_{\text{true}} = e^{-t \cdot K_t} \cdot (f(W_0) - Y_{\text{true}})$$
(47)

$$f(W_t) - Y_{\text{true}} = Qe^{-\Lambda t}Q^T \cdot (f(W_0) - Y_{\text{true}})$$
(48)

$$Q^{T}(f(W_t) - Y_{\text{true}}) = e^{-\Lambda t}Q^{T} \cdot (f(W_0) - Y_{\text{true}}), \tag{49}$$

where Q is matrix of concatenation of eigenfunctions, which behaves a projecting operator, and Λ is diagonal matrix contains non-negative eigenvalues. Additionally, equality in Eq. 48 is due to the property of spectral decomposition, i.e., $e^{K_t} = Qe^{\Lambda}Q^T$.

Eigenvectors compose orthonormal set in \mathbb{R}^N , and each residual components projected in each eigendirection. This directly indicates the convergence speed in each direction in \mathbb{R}^N . For example, we can explictly compute the remained error in direction q_i , denoted as v_i , at timestep t:

$$v_{t,i} = e^{-\lambda_i t} \cdot v_{0,i} \tag{50}$$

- We can observe that once the eigenspace is defined (at the initial state), the eigenvalue governs the training speed in each direction of the basis. Specifically, after an arbitrary time step t, the projected error in the direction corresponding to large eigenvalues decreases exponentially faster than in the case of small eigenvalues.
- Another important aspect is understanding the characteristics of each direction. Empirical and theoretical evidence has shown that the NTK eigenfunctions corresponding to large eigenvalues are low-frequency functions. As a result, neural network training is biased towards reducing error in low-frequency regions (Ronen et al., 2019; Basri et al., 2020; Wang et al., 2021), providing strong evidence of *spectral bias* (Rahaman et al., 2019).
- A natural question arises, "what happens if the eigenvalue is large but the dot product between the corresponding eigenfunction and the residual is small?" This indicates that, despite the large eigenvalue, it contributes less to the reduction of the overall loss. This directly implies that we should consider not only the absolute scale of the eigenvalues but also the dot product (or alignment) between the eigenfunctions and the residual. In summary, we can conclude: if there is high alignment in directions with large eigenvalues, training will be faster.

Based on this analysis, let the timestep \hat{t} that we want to evaluate the loss, then:

$$\hat{Q}^{T}(f(W_{t-\hat{t}}) - Y_{\text{true}}) = e^{-\hat{\Lambda}(t-\hat{t})}\hat{Q}^{T}(f(W_{\hat{t}}) - Y_{\text{true}}). \tag{51}$$

We evaluate the eNTK at every discrete timestep until the training ends. Specifically, we approximate the flow of error over the interval $t - \hat{t} \in [0,1]$. This setting allows the kernel to evolve during training and enables us to further explore the evolution of its eigenspace. For computation of NTKs in our work, we use 'Neural Tangent Library' (Novak et al., 2020).

C.3 Non-Kernel Approach: Analysis via Hessian eigenvalues

Understanding the structure of the Hessian is a crucial aspect in the field of optimization. The Hessian matrix represents the second-order derivatives of the loss function with respect to each parameter, and its eigenvalues provide insights into the local curvature of the model's parameter space. The condition number of the Hessian, defined as $\lambda_{\rm max}/\lambda_{\rm min}$, directly affects the convergence rate and guarantees of quadratic optimization models. In deep learning, the Hessian is widely studied to better understand the complex optimization trajectories of deep neural networks. For instance, Ghorbani et al. (2019) investigated outlier eigenvalues of the Hessian in neural networks (i.e., eigenvalues detached from the main bulk) and demonstrated through empirical and theoretical analysis that such outliers can slow down the convergence of the network.

Building on this line of research, in this section, we present the condition number (CN) of the Hessian during training in three different settings. Fig. 10 illustrates that the CN² of WS-SNF remains significantly lower than that of other comparison models throughout training. This suggests that WS initialization leads to a better-conditioned Hessian not only in the kernel-approximated regime but also in the nonlinear regime, contributing to more efficient training dynamics.

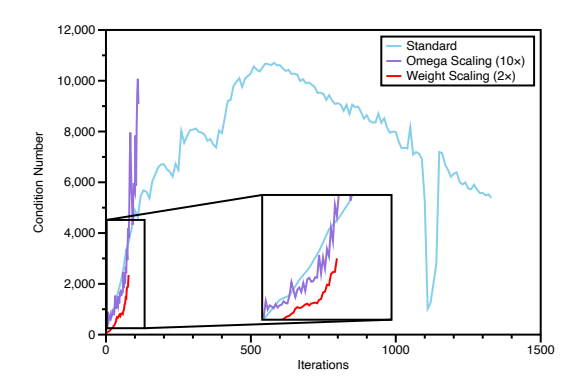


Figure 10. **Condition number of Hessian.** The WS initialization consistently results in a lower condition number compared to other models, indicating that without the approximation of kernelized networks, the optimization path of WS-SNF is well-conditioned.

²For numerical stability, similar to Section 4.3, we compute the average of the top 3 eigenvalues for $\lambda_{\rm max}$ and the bottom 3 eigenvalues for $\lambda_{\rm min}$, where the scale of the eigenvalues are considered in terms of their absolute values. For Hessian computation, we use 'PyHessian' (Yao et al., 2020).

D FREQUENCY SPECTRUM OF 2D IMAGES

Fig. 4 presents a comparative analysis of the frequency spectrum between weight-scaled SNF and 1D audio signals. To further validate our findings, we extend our analysis to Kodak image dataset. Following the methodology of Shi et al. (2022), we partition the frequency map into several discrete bands and compute the mean values within each band.

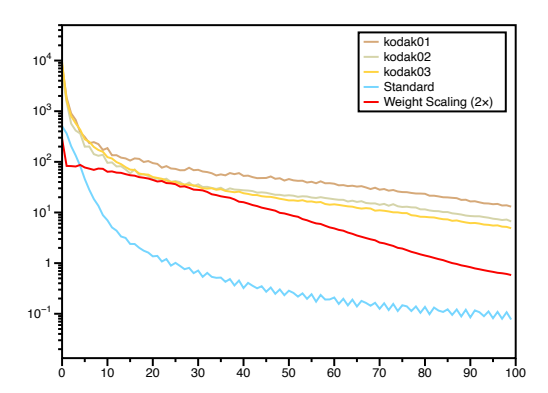


Figure 11. **Frequency distribution of SNFs and 2D signals.** We partition the frequency map into 100 subgroups to facilitate the visualization of 2D signals in a 1D format. Natural images consistently exhibit similar frequency distribution patterns. Notably, WS-SNF demonstrates a better capability in representing high-frequency components, even in its initial state.

Fig. 11 illustrates the frequency distributions across three distinct images from Kodak dataset, as well as the initial output of SNFs. Our analysis reveals that natural images exhibit consistent spectral characteristics across the dataset, providing empirical support for our claim presented in Section 5.2. Moreover, we observe that the initial functional generated by weight-scaled SNF demonstrates a notably higher frequency distribution, consistent with our theoretical analysis.

E EXPERIMENTAL DETAILS AND QUALITATIVE RESULTS

E.1 Training settings and baselines

In this section, we provide detailed information about our experiments. For data fitting tasks, we used the Adam optimizer (Kingma, 2015) with a learning rate of 0.0001, without any learning rate scheduler, except for the occupancy field experiments (in which case, we use PyTorch learning rate scheduler). Each experiment was conducted with 5 different seeds, and we report both the average and standard deviation of the evaluation metric. We note that all baselines in this work are MLP architectures, with slight modifications to the input features or activation functions. We used NVIDIA RTX 3090/4090/A5000/A6000 GPUs for all experiments. Additionally, we set the hyperparameters of each network using a grid search, as shown in Table 2.

ReLU + P.E. (Mildenhall et al., 2020): For this architecture, we use fixed positional encoding applied to the input x, with K frequencies that lift the dimension of the inputs, i.e., $\gamma(x) = (\sin(2^0\pi \cdot x), \cos(2^0\pi \cdot x), \ldots, \sin(2^{K-1}\pi \cdot x), \cos(2^{K-1}\pi \cdot x))$.

FFN (Tancik et al., 2020): For this architecture, we use Gaussian positional encoding applied to the input x, i.e., $\gamma(x) = [\sin(2\pi G \cdot x), \cos(2\pi G \cdot x)]$, where G defines the variance of the Gaussian distribution.

GaussNet (Ramasinghe & Lucey, 2022): For this architecture, we use the Gaussian activation function, i.e., $\sigma(Z) = \exp(-(s \cdot Z)^2)$, where Z denotes the pre-activation matrix and s is a hyperparameter that defines the bandwidth of the Gaussian function.

WIRE (Saragadam et al., 2023): For this architecture, we use a Gabor wavelet-based activation function, i.e., $\sigma(Z) = \exp(j\omega \cdot Z) \exp(-(s \cdot Z)^2)$, where ω and s are hyperparameters.

SIREN (Sitzmann et al., 2020b): We use the sine activation function $\sigma(z) = \sin(\omega \cdot Z)$, where ω in the first layer is a tunable hyperparameter.

Neural field scaling law (Saratchandran et al., 2024): We modify the initialization distribution of the last layer of SIREN, i.e., $W^{(L)} \sim \mathcal{U}\left(-\sqrt{6}/\left(n_{L-1}^{3/4}\omega\right), \sqrt{6}/\left(n_{L-1}^{3/4}\omega\right)\right)$, where n_{L-1} denotes the width of the (L-1)-th layer.

Xavier uniform initialization (Glorot & Bengio, 2010): In this case, we use the standard Xavier uniform initialization for the SNF architecture, i.e., $W^{(l)} \sim \mathcal{U}\left(-\sqrt{6}/\sqrt{n_{l-1}+n_l},\sqrt{6}/\sqrt{n_{l-1}+n_l}\right)$, $l \in [1,L]$.

Table 2. **Detailed information about hyperparameters.** We provide the exact hyperparameter settings for each domain in the table below. 'default' in ReLU+P.E. denotes the using nyquist sampling methods (Saragadam et al., 2023).

	ReLU+P.E.	FFN		SIREN	GaussNet	WI	RE	Weight scaling
	k	σ	m	ω	s	ω	s	α
Image	10	10	256	30	10	20	10	2.37
Occ. Field	default	2	10	10	10	10	40	3.7
Spherical Data	default	2	256	30	10	10	20	2.5
Audio	default	20	20	3000	100	60	10	2.0

E.2 NEURAL DATASET EXPERIEMENTS

In recent research on constructing large-scale NF datasets (Ma et al., 2024; Papa et al., 2024), there has been growing interest in this area. However, no studies have investigated how initialization schemes affect the overall process, from constructing SNF-based neural datasets to their application in downstream tasks. To address this gap, we first measure the time required to fit the entire dataset to NFs and then report the classification accuracy on the neural dataset while varying the scale factor α . The results are shown in Table 3.

Analysis. Interestingly, despite the efficiency of WS-SNFs in terms of training time (i.e., the time required to fit each datum into an individual NF until reaching the target PSNR), the test accuracy (i.e., classification accuracy on the test set SNFs), specifically for the case of $\alpha=1.5$, does not significantly decrease. Moreover, we observed that, in the case of $\alpha=2.0$, test accuracy dropped by an average of 5 percentage points across all PSNR values. This mirrors a similar phenomenon discussed in Papa et al. (2024), where constraining the weight space of NFs was identified as a key factor in downstream task performance. More precisely, scaling initialization distributions causes the neural functions to lie in a larger weight space, making it harder to learn features from the weights. Furthermore, we propose an interesting research direction: can we create a neural dataset quickly without compromising the performance of downstream tasks and without incurring additional cost?

Experimental details. For training, we used 'fit-a-nef' (Papa et al., 2024), a JAX-based library for fast construction of large-scale neural field datasets. We used the entire dataset for NF dataset generation (*i.e.*, 60,000 images for MNIST and CIFAR-10, respectively). Additionally, we used an MLP-based classifier targeted at classifying each NF's class, which consists of 4 layers and a width of 256, and was trained with cross-entropy loss for 10 epochs.

Table 3. **Neural dataset experiments.** Each neural dataset is trained until it reaches the batch-averaged **target PSNR**. The **training time** refers to the total time required to construct the entire INR dataset. A classifier is then trained on the neural dataset, and the resulting **test accuracy** is reported for each configuration. We use SIREN as the NF architecture, which is a widely used baseline in this area.

		Neural	MNIST	Neural CIFAR-10		
	Target PSNR	Training time	Test accuracy	Training time	Test accuracy	
	35	14m 23s	97.95±0.00	19m 14s	47.98±0.01	
SIREN	40	18m 20s	97.76 ± 0.00	29m 45s	48.46 ± 0.01	
	45	23m 23s	97.53 ± 0.01	47m 54s	48.09 ± 0.01	
	35	7m 22s	97.56 ± 0.00	10m 52s	47.15 ± 0.02	
WS (\times 1.5)	40	8m 22s	97.81 ± 0.00	17m 21s	47.72 ± 0.01	
	45	10m 41s	97.02 ± 0.01	25m 52s	46.08 ± 0.03	
	35	5m 25s	97.48 ± 0.01	8m 26s	43.30±0.02	
WS (\times 2.0)	40	5m 32s	97.06 ± 0.01	9m 20s	42.86 ± 0.02	
	45	5m 41s	97.49 ± 0.00	10m 51s	42.70 ± 0.01	

E.3 TRAINING FOR ADDITIONAL ITERATIONS

Weight scaling initialization primarily focuses on the training efficiency of neural fields. In other words, the experiments in the main paper were conducted over a limited number of epochs. In this subsection, we provide qualitative results from models trained for additional iterations. As shown in Table 4, networks with WS initialization continue to outperform other networks, suggesting that its effectiveness is consistently preserved throughout the training process.

		Image (300 iterations)		Occ. Field (100 iterations)	Spherical Data (15k iterations)	Audio (5k iterations)	
	Activation	KODAK	DIV2K	Lucy	ERA5	Bach	
Xavier Uniform (Glorot & Bengio, 2010)	Sinusoidal	2.31	2.20	0.0706	7.10±1.02	16.16	
ReLU + P.E. (Mildenhall et al., 2020)	ReLU	21.77	19.60	0.9920	41.32 ± 0.16	32.40	
FFN (Tancik et al., 2020)	ReLU	26.51	25.62	0.9874	45.27±0.12	17.54	
SIREN init. (Sitzmann et al., 2020b)	Sinusoidal	26.01	24.76	0.9926	44.42 ± 0.32	46.78	
GaussNet (Ramasinghe & Lucey, 2022)	Gaussian	21.90	20.22	0.9935	44.15±0.12	34.65	
WIRE (Saragadam et al., 2023)	Wavelet	31.47	30.89	0.9939	45.13±0.42	20.17	
NFSL (Saratchandran et al., 2024)	Sinusoidal	26.91	25.97	0.9933	45.10 ± 0.08	45.70	
Weight scaling (ours)	Sinusoidal	52.73	53.10	0.9950	49.63±0.14	54.04	

Table 4. **Quantitative results:** training for additional iterations.

E.4 QUALITATIVE RESULTS

In this subsection, we provide qualitative results of experiments in Section 5.1. We do not provide reconstructed results for occupancy field reconstruction with Xavier initialization case due to training failure.

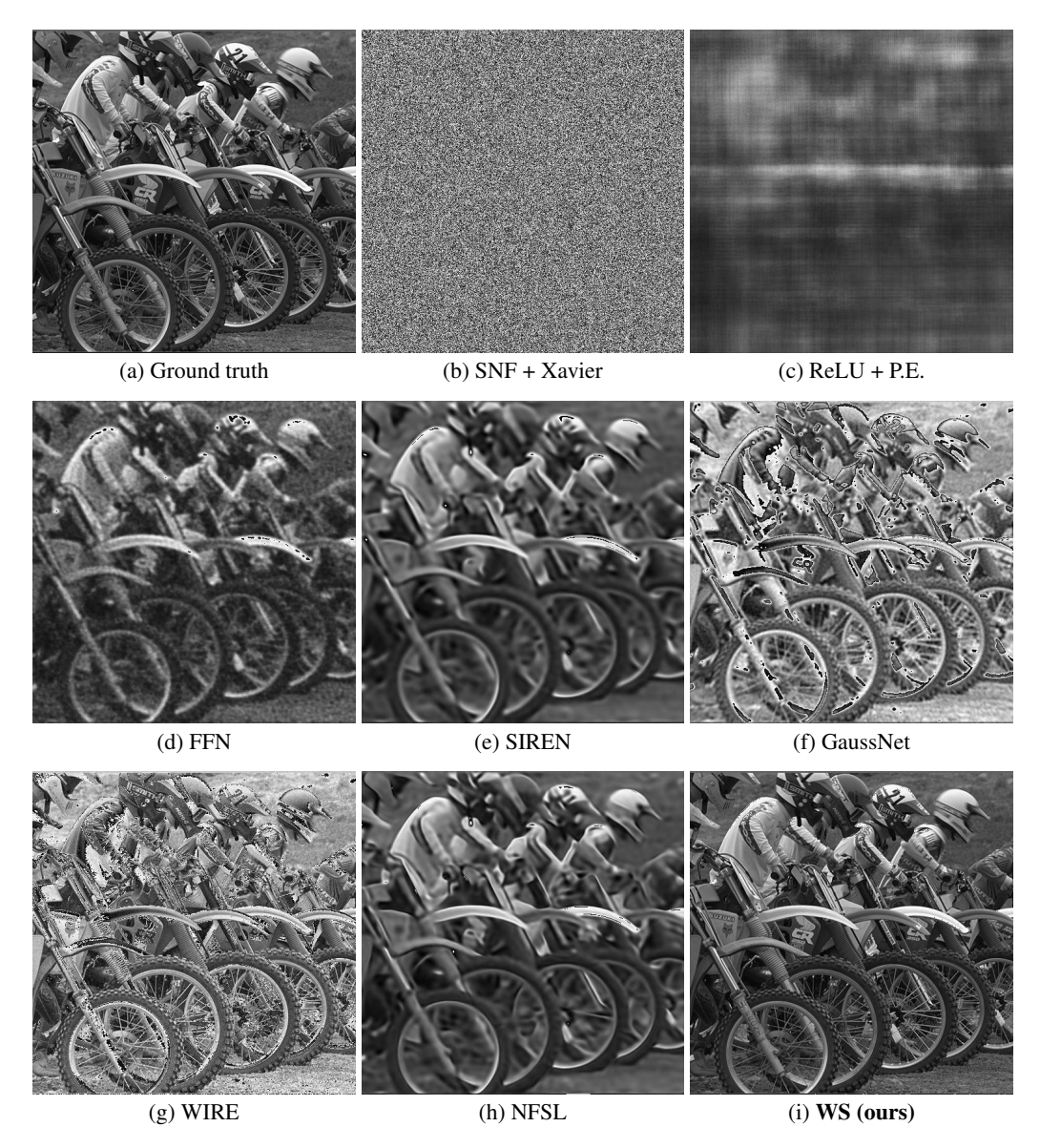


Figure 12. **Image reconstruction**: qualitative results.

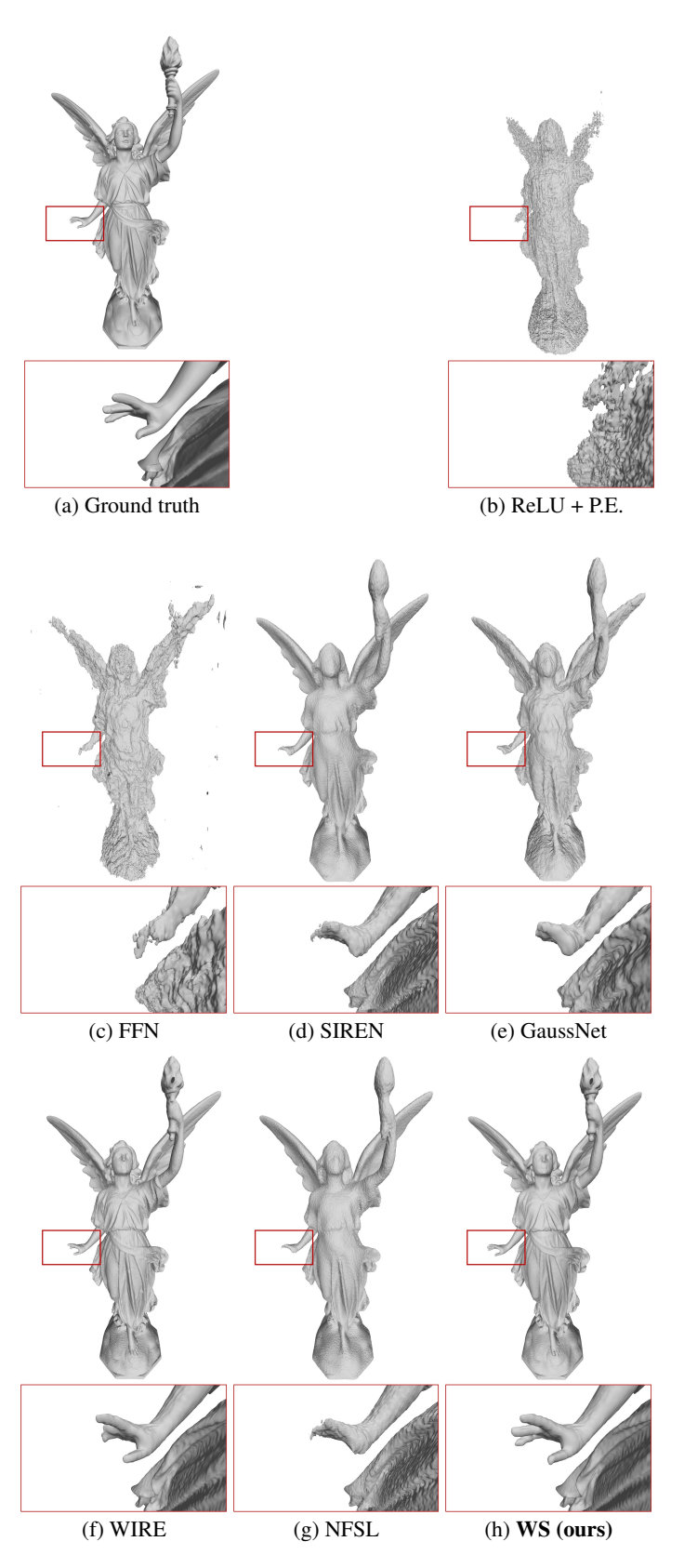


Figure 13. Occupancy field experiments: qualitative results.

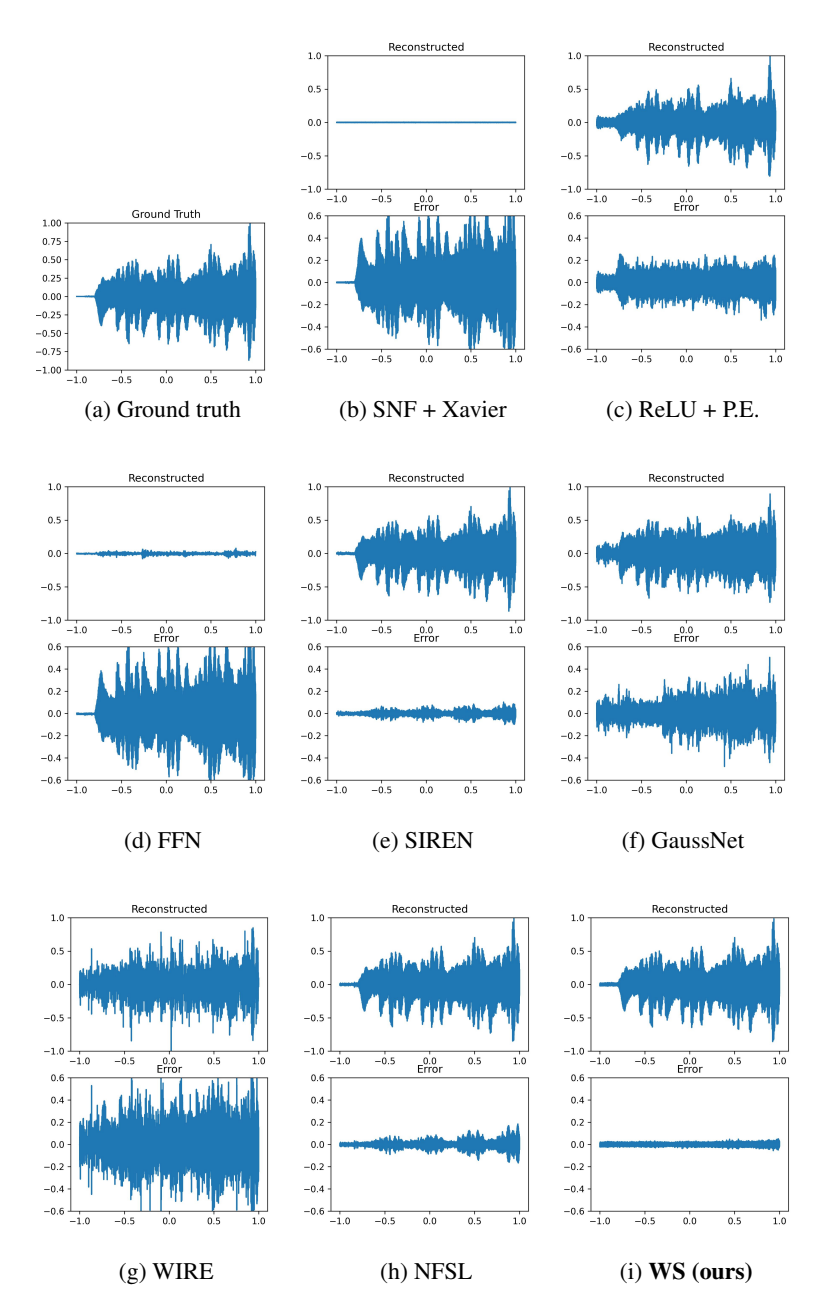


Figure 14. Audio reconstruction: qualitative results.

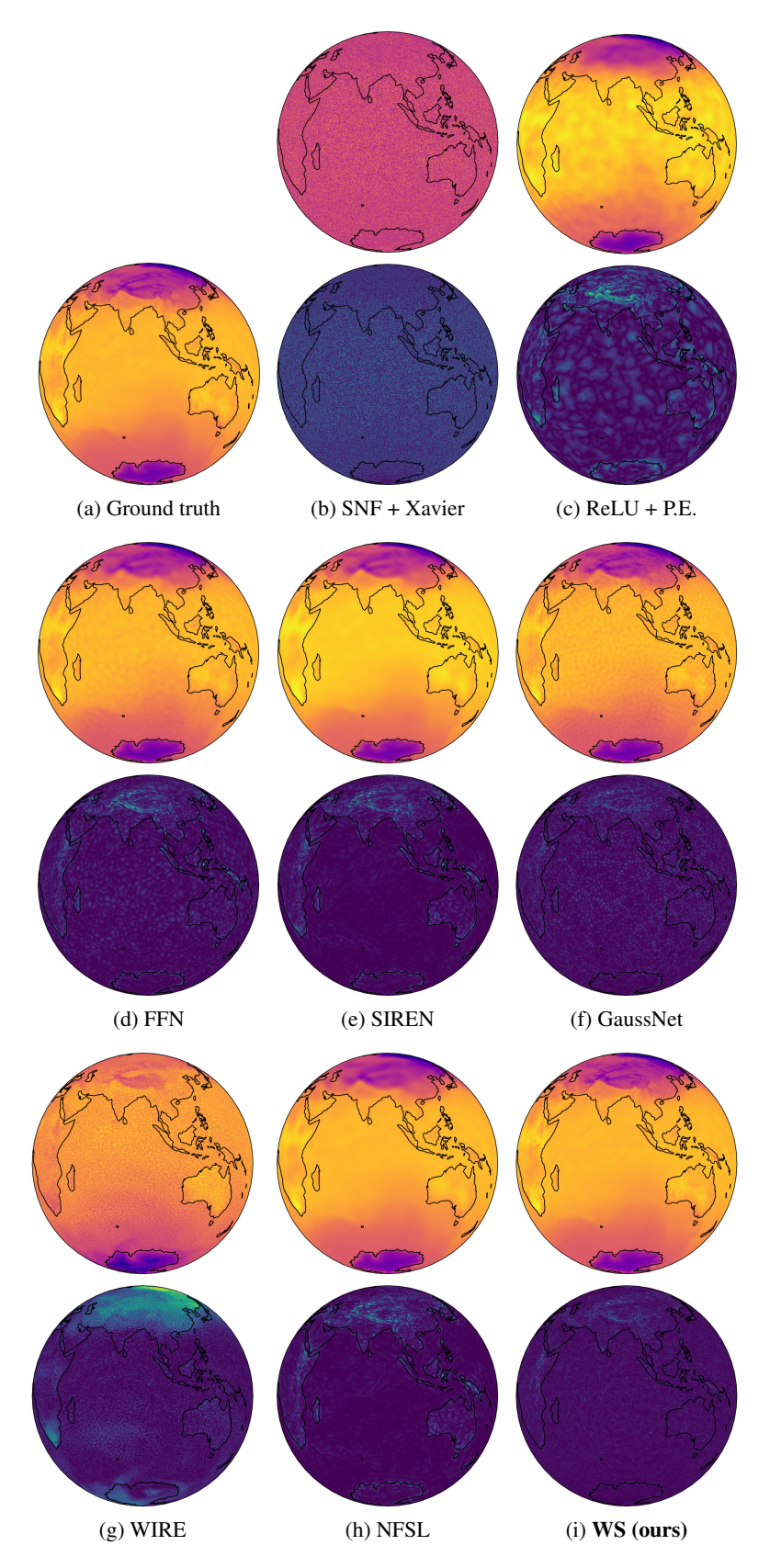


Figure 15. **Spherical data reconstruction**: qualitative results. The top figure of each index shows the reconstructed results, while the bottom figure of each index shows the error map.